HYPERSONIC, LOW DENSITY FLOW PAST A WEDGE OF FINITE LENGTH

A THESIS

Presented to

The Faculty of the Division of Graduate Studies and Research

By

Francis Joaquin Klemm

In Partial Fulfillment

of the Requirements for the Degree

Doctor of Philosophy

in the School of Aerospace Engineering

Georgia Institute of Technology

June 1975

HYPERSONIC, LOW DENSITY FLOW PAST A WEDGE OF FINITE LENGTH

Approved:

Don P. Giddens, Chairman

Louis H. Banger

James E. Hubbart

Date approved by Chairman: 4/25/75

ACKNOWLEDGMENTS

I would like to acknowledge the many people who helped in making this thesis possible. Of foremost help was Dr. Don P. Giddens, my faculty advisor. His assistance and guidance, not only in this project, but throughout my years at Georgia Tech are greatly appreciated.

I am also indebted to the Reading Committee, Dr. Don P. Giddens, Dr. Louis H. Bangert, and Professor James E. Hubbart, for their suggestions and careful examination of this manuscript.

In addition I wish to acknowledge the assistance of my friends and colleagues. I thank Mr. M. S. Padmanabhan, with whom I had many helpful hours of discussion; Mr. Robert L. Roach for his generous assistance in the graphic displays contained within the text; and Mr. Walter "Rob" Robinson, whose helpfulness in the computer center greatly expedited the completion of this dissertation. Furthermore, I acknowledge the expert skills of Mrs. Carolyn Piersma, who typed the final draft.

I greatly appreciate the financial aid provided me by an NDEA Fellowship and an institutional research assistantship.

Special thanks are also extended to my parents and especially my father. Although he did not live to see the completion of this work, he was a great inspiration to the author.

A debt of sincere gratitude is owed to my wife, Pamela. Over the years her patience, understanding, and support have been the keystone in making my college education possible.

TABLE OF CONTENTS

Page

ACKNOWLEDGMENTS ii

LIST OF TABLES v

LIST OF ILLUSTRATIONS vi

LIST OF SYMBOLS viii

SUMMARY xi

Chapter

I. INTRODUCTION 1

History and Review
Purpose and Method of Research

II. FORMULATION 7

Governing Equations
Outer Boundary Conditions
Symmetry Conditions
Surface Boundary Conditions

III. NUMERICAL METHODS OF SOLUTION 17

Solution of the Equations
Macroscopic Properties
Incorporation of the Boundary Conditions
Overall Method
Convergence and Stability of the Numerical Scheme
Accuracy of the Numerical Scheme

IV. RESULTS 31

Flow Field Specifications
Macroscopic Property Profiles
Surface Variations
Comparison with Experiment

Chapter Page

V. CONCLUSIONS 63

APPENDIX

A. DISCRETE ORDINATE METHOD. 67

B. DERIVATION OF CHARACTERISTICS 69

C. SOLUTION GRID NETWORK. 73

D. INFERENCE OF WALL PRESSURE FROM THE WALL NUMBER DENSITY COEFFICIENT 77

BIBLIOGRAPHY 79

VITA 82

LIST OF TABLES

Table — Page

1. The X-Grid Lines 74
2. The Y-Grid Lines 75
3. The Coordinates of the Surface Grid Points 76

LIST OF ILLUSTRATIONS

Figure		Page
1.	Hypersonic Flow Past a Body with a Sharp Leading Edge . .	2
2.	Geometry and Coordinate System for the Wedge Flow Problem.	8
3.	A Grid System with a Related Characteristic Line. . . .	20
4.	Hypersonic Flow Field About a "Transparent" Wedge . . .	28
5.	Number Density, $x < 33.50$	34
6.	Number Density in the Vicinity of the Leading Edge . . .	35
7.	Number Density, $33.50 \leq x < 64.437$	36
8.	Number Density, $x \geq 64.437$	37
9.	X-Velocity, $x < 33.50$.	40
10.	X-Velocity, $33.50 \leq x < 64.437$.	41
11.	X-Velocity, $x \geq 64.437$	42
12.	Y-Velocity, $x < 33.50$.	44
13.	Y-Velocity, $33.50 \leq x < 64.437$.	45
14.	Y-Velocity, $x \geq 64.437$	46
15.	Temperature, $x < 33.50$	48
16.	Temperature, $33.50 \leq x < 64.437$	49
17.	Temperature, $x \geq 64.437$	50
18.	Variation of the Number Density at the Surface	53
19.	Variation of the Tangential Velocity at the Surface. . .	55
20.	Variation of the Gas Temperature at the Surface	56
21.	Variation of the Wall Number Density Coefficients Along the Surface	57

Figure Page

22. Wall Pressure 59

23. Number Flux. 61

LIST OF SYMBOLS

d	distance along the slant surface
D	notation for d employed in figures
f	local distribution function
F	local Maxwellian equilibrium distribution function
g	first reduced distribution function
G	first reduced equilibrium distribution function
g_w	first reduced wall distribution function
h	second reduced distribution function
H	second reduced equilibrium distribution function
I	collision integral
k	Boltzmann constant
L	wedge length
m	molecular mass
M	Mach number
n	number density
N	notation for n employed in figures
N_f	number flux
NF	notation for N_f employed in figures
n_w	wall number density coefficient
NW	notation for n_w employed in figures
p	pressure
P	physical property; also notation for p employed in figures
R	universal gas constant (k/m)
s	exponent for viscosity power law

T	temperature
T_w	wall temperature
u	macroscopic velocity
UT	tangential velocity
UX	notation for u_x employed in figures
UY	notation for u_y employed in figures
v	microscopic velocity
v_n	normal microscopic velocity ($v_x \sin \alpha - v_y \cos \alpha$)
V_∞	characteristic velocity ($\sqrt{2RT_\infty}$)
w	quadrature weight
x	Cartesian coordinate
X	notation for x employed in figures
y	Cartesian coordinate
Y	notation for y employed in figures
α	wedge half-angle
β	characteristic curve
γ	defined by Equation B-4
θ	arbitrary property
λ_∞	free-stream mean free path
Λ	functional of g and h
μ	viscosity coefficient
ν	collision frequency
ϕ	function of v_x and v_y

Superscripts

^	dimensional quantity

Subscripts

a	starting point for characteristic integration
FM	free molecular
i	integer indicating an x-grid point
ir	incoming towards the rear surface
is	incoming towards the slant surface
j	integer indicating a y-grid point
k	integer indicating a discrete v_x
k_e	integer indicating the largest discrete v_x
k_{0^-}	integer indicating the negative discrete v_x with smallest magnitude
k_{0^+}	integer indicating smallest positive discrete v_x
ℓ	integer indicating a discrete v_y
ℓ_e	integer indicating the largest discrete v_y
ℓ_{0^-}	integer indicating the negative discrete v_y with smallest magnitude
ob	outer boundary
r	rear surface
s	slant surface
x	x-component
y	y-component
z	z-component
o	stagnation condition
∞	free-stream condition

SUMMARY

The macroscopic properties of the flow field surrounding a symmetric wedge of finite length immersed in a low density hypersonic stream of a monatomic gas have been determined by solving the Boltzmann transport equation with the Bhatnagar-Gross-Krook model for the collision integral. The numerical technique employed in this solution was the discrete ordinate method with a trapezoidal integration along molecular path lines, thus providing an accurate determination of effects of directionality of the molecules. The influence due to the upstream velocity component of random molecular motion is preserved by such an approach and by prescribing boundary conditions over a surface completely enclosing the flow field of interest.

The solution method yields the molecular velocity distribution function throughout the flow, from which macroscopic properties such as density, velocity, and temperature are determined. Effects created by the upstream influence are clearly evident in these properties, particularly in the regions ahead of the leading and trailing edges. Although the primary computational emphasis was placed on the solution near the forebody of the wedge, reasonably accurate results were obtained in the wake region.

Due to the lack of published measurements, a realistic comparison of theory and experiment can be made only with the slant surface wall pressures. For this quantity the computed values compare favorably with data obtained from wind tunnel studies. Calculated results for

other macroscopic variables are in general agreement with trends shown in measurements about flat plates. However, a strict quantitative comparison for wedge flows must await the advent of new experimental data.

The principal drawback of the method is the substantial computer time required. Yet the results indicate that if one is willing to expend the large computer times involved, then there is a reasonable assurance of obtaining satisfactory solutions for other simple body shapes.

CHAPTER I

INTRODUCTION

History and Review

Hypersonic, low density flow past a shape with a sharp leading edge may be characterized by several different regimes. Referring to Figure 1, the first regime encountered is that of near free molecular flow. In this region collisions of molecules with each other are negligible and the flow field is predominately determined by the interaction between molecules and the surface of the body. Following this zone is the transition regime where the intermolecular and surface-molecular interactions assume equal importance in the establishment of flow properties. Further downstream, the flow enters the merged layer where intermolecular interactions begin to dominate. The merged layer is characterized by the fact that the shock wave thickness is of a size comparable to the shock layer. Theoretical studies predict that both a temperature jump and velocity slip exist at the wall for each of the above flows. Finally, the hypersonic interaction regime is encountered. This is generally subdivided into strong and weak interactions. For the strong interaction case the induced pressure caused by the boundary layer displacement must be considered to be coupled with the displacement, whereas in the weak interaction regime the coupling is considered negligible and is disregarded.

These various regimes fall into two basic analytic divisions, the kinetic and continuum regions. The kinetic region is generally

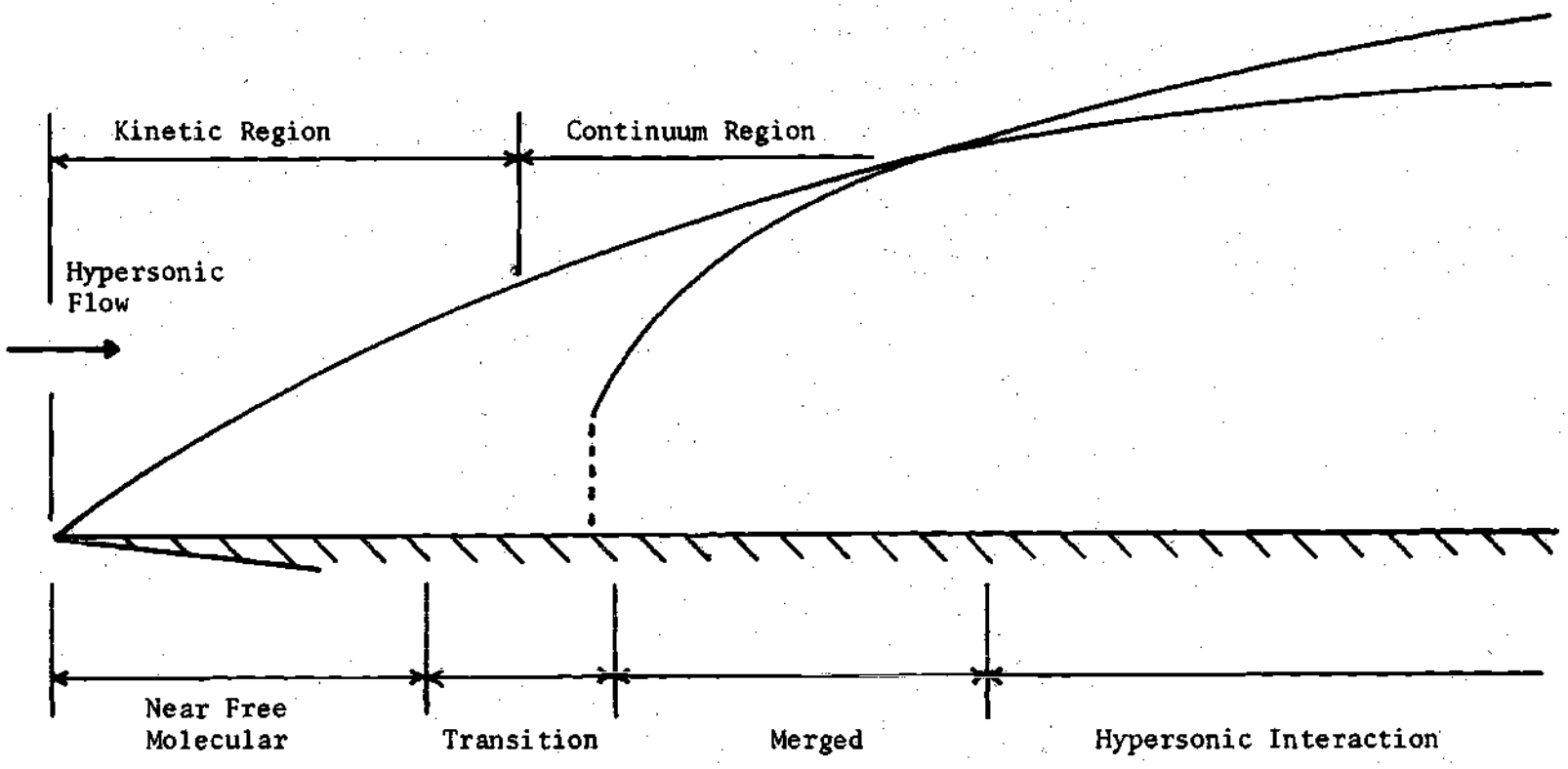

Figure 1. Hypersonic Flow Past a Body with a Sharp Leading Edge

considered to be the near free molecular regime and a portion of the transition region. In these zones a molecular approach to the gas flow problem is necessary to obtain solutions for the flow field properties. In the continuum region, which follows downstream, the concepts and equations of continuum gas dynamics (e.g., the Navier-Stokes equations) are generally adequate in obtaining the basic details of the flow; consequently, they are often used. The fact that the continuum equations describe the flow downstream does not imply that a molecular approach is invalid in this region; on the contrary such a method is applicable throughout the entire flow field.

Studies of the hypersonic flow field over a sharp leading edge have usually been concerned with flow over a flat plate because of the simplicity of geometry. Experimental studies include surface heat transfer,[1,2] slip velocity,[3] and pressure[4,5,6,7] measurements and the determination of velocity[4] and density[8,9] profiles. Also, the Boltzmann equation and extensions of the continuum equations have been solved[10,11,12,13,14] for flows near the leading edge.

The flow field about the leading edge of a wedge has come under rather limited experimental[2,7,15,16] and theoretical[12,17,18] study. Although a few surface pressure measurements,[2,7,15,16] density,[7] and velocity profiles[7] have been published, the accuracy of much of the data[2,16] for flow over wedges must be questioned, especially in the near proximity of the leading edge. This is due to the fact that in many cases the data presented were not obtained from flow about a wedge but from flat plates inclined at angles of attack. While this would appear satisfactory from a continuum approach, kinetic theory shows

that the results near the leading edge may be quite severely affected by such an approach. This is caused by an extensive flux of molecules propagating upstream from the undersurface of the plate and influencing the upper surface. The momenta and energies associated with these molecules will differ from those found in the flow over a wedge.

Analytical studies of flow over a wedge are more complex than for the flat plate due to the additional flow turning or compression and the inclined shape of the boundaries which the wedge presents. Theoretical approaches include continuum methods such as Cheng's strong interaction theory[12] and the theory of Chow and Eilers,[18] and molecular methods such as the Monte Carlo simulation of the Boltzmann equation carried out by Vogentiz, et al.[17]

Purpose and Method of Research

The purpose of this research has been to develop a general method for the solution of the flow properties about a symmetric finite length wedge immersed in a low density, hypersonic flow. The principal interest is in determining the flow field in the immediate neighborhood of the body. The approach that has been taken is to obtain a solution to the Boltzmann equation using the discrete ordinate method with integration along characteristic lines. The discrete ordinate method was applied by Giddens[19] to the linearized Boltzmann equation where it has been shown to be suitable for obtaining the macroscopic properties of low density flows over a wide range of Knudsen numbers. These different Knudsen numbers cover the range of the various flow regimes encountered on the wedge. The method has also been used by several researchers[13,14,20,21,22,23,24] in recent years to obtain the solution

for flow about a mathematically thin flat plate. Except for Reference 14, these solutions were obtained by applying some form of Cartesian differencing techniques to the Boltzmann equation and solving the resultant difference equations. In the paper by Giddens and Huang,[14] the Boltzmann equation was solved by a difference technique with reference to a set of characteristic lines which were shown to be molecular path lines. This technique provides for a more accurate method of accounting for the zones of influence in the flow field. By following the molecular path line a property of the molecule is determined not only by the properties of the adjacent points, as in the weighted average techniques of the Cartesian difference schemes, but also by the properties of the origination point of the molecule.

A closed boundary type approach is employed in order to account for the flux of molecules propagating upstream due to random motion. An initial value approach in which the solution marches downstream[20,21,22] fails to account for this backward flux of molecules, which has been shown both experimentally and analytically to play an important role in the determination of flow properties.

A survey of the available data for low density wedge flow indicated that the majority of the experiments were performed at Mach numbers near 20 in diatomic gases. Previous experience in applying the discrete ordinate method to flows over flat plates showed that lengthy computer time would be required for the wedge problem. Consequently, a solution for a diatomic gas with internal degrees of freedom was immediately ruled out because the complexity of the collision model requires an additional independent variable, the quantum level of the diatomic

molecule. Furthermore, consideration of a Mach number near 20 would require an extremely large number of discrete velocity points to attain sufficient accuracy in the solution, causing a substantial increase in computer time. Since an objective of the research was to extend the discrete ordinate method to a more practical shape than previously attempted, it was believed that this could best be accomplished within the framework of available computer time by examining a moderately high hypersonic Mach number. The basic purpose of the research would thus be met by such a solution, and the feasibility of the method for other rarefied flow field calculations could be evaluated.

CHAPTER II

FORMULATION

Governing Equations

The geometry of the problem is shown in Figure 2. A symmetric wedge with half-angle α and length $\hat{L}$ is immersed in the hypersonic flow of a monatomic gas with a free-stream Mach number M_∞. The wall is assumed to have a constant temperature $\hat{T}_w$ and the wedge is at zero angle of attack. The problem is two-dimensional in physical space, and external forces are considered negligible. The defining equation for the flow is assumed to be the Boltzmann equation with the Bhatnagar-Gross-Krook (BGK) approximation[25] used to replace the collision integral:

$$\hat{v}_x \frac{\partial \hat{f}}{\partial \hat{x}} + \hat{v}_y \frac{\partial \hat{f}}{\partial \hat{y}} = \hat{\nu}(\hat{F} - \hat{f}) \tag{2-1}$$

$$\hat{f} = \hat{f}(\hat{x},\hat{y},\hat{v}_x,\hat{v}_y,\hat{v}_z)$$

$$\hat{F} = \hat{n}\left(\frac{1}{2\pi R\hat{T}}\right)^{3/2} \exp\left\{-\frac{1}{2R\hat{T}}\left[(\hat{v}_x - \hat{u}_x)^2 + (\hat{v}_y - \hat{u}_y)^2 + \hat{v}_z^2\right]\right\} \tag{2-2}$$

where

$$\hat{\nu} = \frac{\hat{n}k\hat{T}}{\hat{\mu}} \tag{2-3}$$

Here, a right-handed set of Cartesian axes is taken with the x-axis lying along the center line of the wedge in the direction of

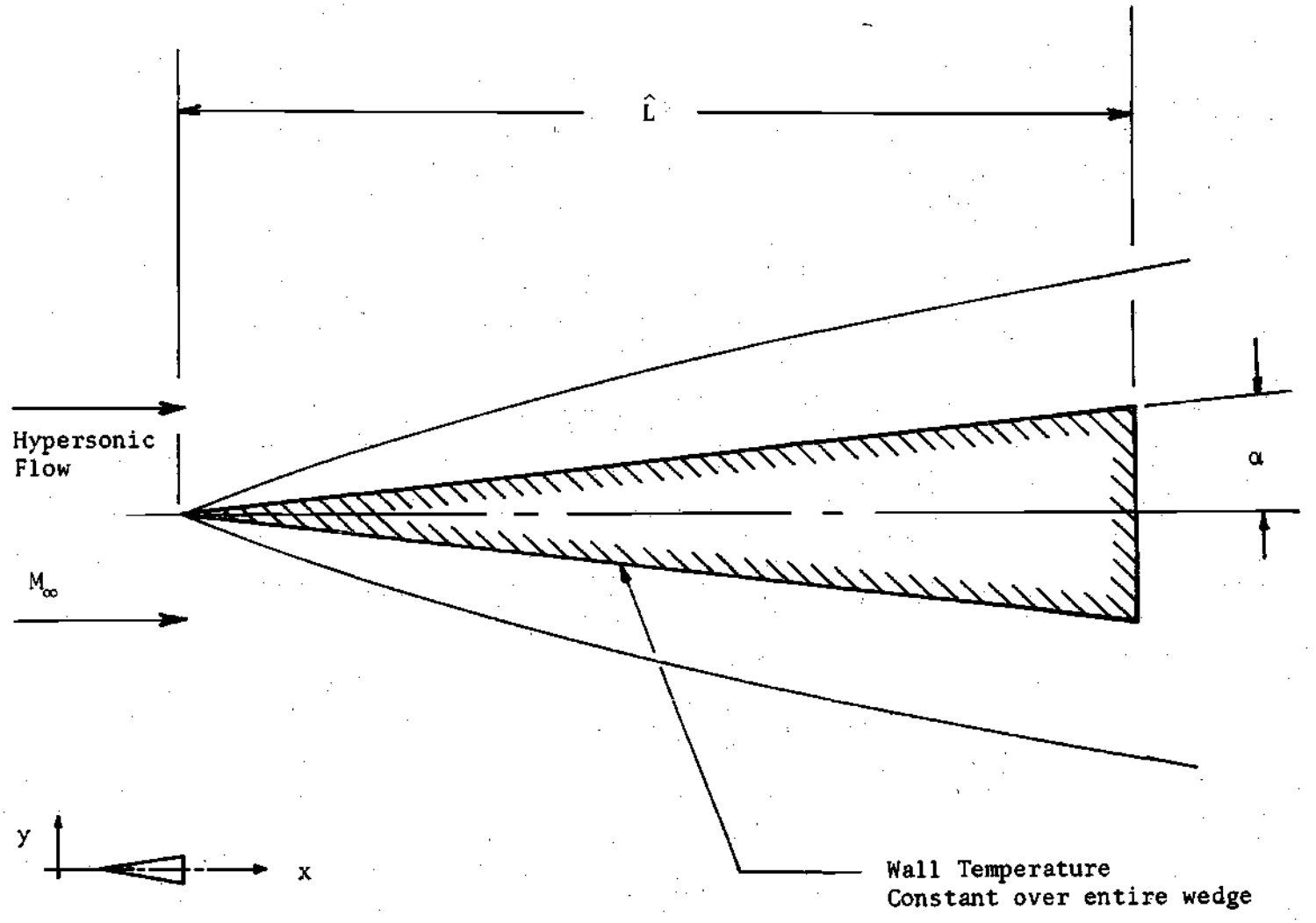

Figure 2. Geometry and Coordinate System for the Wedge Flow Problem

the oncoming free stream. The BGK model has been chosen because of the simplicity which it provides in the numerical solution of the problem, while maintaining a form representative of the actual process taking place in the collision integral. This model has been used by previous investigators[13,14] who have demonstrated that it is sufficiently accurate to obtain the general trends for low density flows similar to wedge flows.

In the present analysis a power law temperature dependence is assumed for the viscosity coefficient

$$\frac{\hat{\mu}}{\hat{\mu}_\infty} = \left(\frac{\hat{T}}{\hat{T}_\infty}\right)^s \tag{2-4}$$

The free-stream viscosity coefficient, $\hat{\mu}_\infty$, is related to the free-stream number density, temperature, and mean free path by

$$\hat{\mu}_\infty = \frac{5}{16} m\hat{n}_\infty \lambda_\infty (2\pi R\hat{T}_\infty)^{\frac{1}{2}} \tag{2-5}$$

Upon combining Equations (2-3), (2-4), and (2-5) the collision frequency is given by

$$\hat{\nu} = \frac{16}{5} \frac{\hat{n}R\hat{T}}{\hat{n}_\infty \lambda_\infty} (2\pi R\hat{T}_\infty)^{-\frac{1}{2}} \left(\frac{\hat{T}}{\hat{T}_\infty}\right)^{-s} \tag{2-6}$$

To reduce the computer storage requirement for the problem, the functional dependence of Equation (2-1) on $\hat{v}_z$ is eliminated by a suitable integration. The computation of the physical properties is facilitated by requiring two different integrations of Equation (2-1). The

first involves integration with respect to $\hat{v}_z$ while in the second, the equation is multiplied by $\hat{v}_z^2$ before integrating. The reduced equations and distribution functions are then given by

$$\hat{v}_x \frac{\partial \hat{g}}{\partial \hat{x}} + \hat{v}_y \frac{\partial \hat{g}}{\partial \hat{y}} = \hat{\nu}(\hat{G} - \hat{g}) \tag{2-7}$$

$$\hat{v}_x \frac{\partial \hat{h}}{\partial \hat{x}} + \hat{v}_y \frac{\partial \hat{h}}{\partial \hat{y}} = \hat{\nu}(\hat{H} - \hat{h}) \tag{2-8}$$

where

$$\hat{g} = \hat{g}(\hat{x},\hat{y},\hat{v}_x,\hat{v}_y) = \int_{-\infty}^{\infty} \hat{f}\, d\hat{v}_z \tag{2-9}$$

$$\hat{G} = \frac{\hat{n}}{2\pi R\hat{T}} \exp\left\{ - \frac{1}{2R\hat{T}} \left[(\hat{v}_x - \hat{u}_x)^2 + (\hat{v}_y - \hat{u}_y)^2 \right] \right\} \tag{2-10}$$

$$\hat{h} = \hat{h}(\hat{x},\hat{y},\hat{v}_x,\hat{v}_y) = \int_{-\infty}^{\infty} \hat{v}_z^2\, \hat{f}\, d\hat{v}_z \tag{2-11}$$

$$\hat{H} = R\hat{T}\hat{G} \tag{2-12}$$

The macroscopic properties (i.e., number density, x-velocity component, y-velocity component, and temperature) in terms of $\hat{g}$ and $\hat{h}$, are then

$$\hat{n} = \int_{-\infty}^{\infty} \int_{-\infty}^{\infty} \hat{g}\, d\hat{v}_x\, d\hat{v}_y \tag{2-13}$$

$$\hat{u}_x = \frac{1}{\hat{n}} \int_{-\infty}^{\infty} \int_{-\infty}^{\infty} \hat{v}_x \hat{g}\, d\hat{v}_x d\hat{v}_y \tag{2-14}$$

$$\hat{u}_y = \frac{1}{\hat{n}} \int_{-\infty}^{\infty} \int_{-\infty}^{\infty} \hat{v}_y \hat{g} \, d\hat{v}_x \, d\hat{v}_y \tag{2-15}$$

$$\hat{T} = \frac{1}{3\hat{n}R} \left\{ \int_{-\infty}^{\infty} \int_{-\infty}^{\infty} \hat{h} \, d\hat{v}_x d\hat{v}_y \right. \tag{2-16}$$

$$\left. + \int_{-\infty}^{\infty} \int_{-\infty}^{\infty} \left[(\hat{v}_x - \hat{u}_x)^2 + (\hat{v}_y - \hat{u}_y)^2 \right] \hat{g} \, d\hat{v}_x d\hat{v}_y \right\}$$

The solution to the problem of finding the macroscopic properties has now been transformed into solving Equations (2-7) and (2-8) for $\hat{g}$ and $\hat{h}$, and performing the appropriate moments as given in Equations (2-13) through (2-16).

A characteristic velocity V_∞ is introduced

$$V_\infty = (2R\hat{T}_\infty)^{\frac{1}{2}}$$

and Equations (2-7) through (2-16) are nondimensionalized as indicated below:

$$x = \frac{\hat{x}}{\lambda_\infty} \qquad y = \frac{\hat{y}}{\lambda_\infty} \qquad v_x = \frac{\hat{v}_x}{V_\infty}$$

$$v_y = \frac{\hat{v}_y}{V_\infty} \qquad n = \frac{\hat{n}}{\hat{n}_\infty} \qquad u_x = \frac{\hat{u}_x}{V_\infty}$$

$$u_y = \frac{\hat{u}_y}{V_\infty} \qquad T = \frac{\hat{T}}{\hat{T}_\infty} \qquad \nu = \frac{\hat{\nu} \, \lambda_\infty}{V_\infty}$$

$$g = \frac{\hat{g} \, V_\infty^2}{\hat{n}_\infty} \qquad G = \frac{\hat{G} \, V_\infty^2}{\hat{n}_\infty} \qquad h = \frac{\hat{h}}{\hat{n}_\infty}$$

$$H = \frac{\hat{H}}{\hat{n}_\infty}$$

The discrete ordinate method is then applied to the nondimensional forms of Equations (2-7) and (2-8).

$$v_k \frac{\partial g_{k,\ell}}{\partial x} + v_\ell \frac{\partial g_{k,\ell}}{\partial y} = \nu(G_{k,\ell} - g_{k,\ell}) \tag{2-17}$$

$$v_k \frac{\partial h_{k,\ell}}{\partial x} + v_\ell \frac{\partial h_{k,\ell}}{\partial y} = \nu(H_{k,\ell} - h_{k,\ell}) \tag{2-18}$$

where

$$g_{k,\ell} = g(x,y;v_k,v_\ell)$$

and

$$h_{k,\ell} = h(x,y;v_k,v_\ell)$$

The method is such that g and h are obtained, not as continuous functions of v_x and v_y but, at certain discrete velocity points. That is, g and h are parameterized by $v_x = v_k$ and $v_y = v_\ell$ ($k = 1,\ldots,k_e$; $\ell = 1,\ldots,\ell_e$). It should be noted that g and h remain continuous in x and y. A further discussion of the method is given in Appendix A.

An analysis of Equations (2-17) and (2-18) reveals that there exists a characteristic line given by

$$\left(\frac{dy}{dx}\right)_{char} = \frac{v_\ell}{v_k} \tag{2-19}$$

This can be introduced to further reduce these equations to

$$v_k \frac{dg_{k,\ell}}{dx} = \nu(G_{k,\ell} - g_{k,\ell}) \tag{2-20}$$

$$v_k \frac{dh_{k,\ell}}{dx} = \nu(H_{k,\ell} - h_{k,\ell}) \tag{2-21}$$

A derivation of this transformation is presented in Appendix B.

The characteristic line given by Equation (2-19) represents a molecular path line for a specific velocity pair. It is along this line that a molecule transfers its properties. An analogy exists in continuum flow where a "fluid element" transmits its properties along streamlines, and these are also characteristic lines.

The solution for g and h is obtained by solving the simultaneous Equations (2-19), (2-20), and (2-21) with appropriate boundary conditions. These are of three types: the outer boundary conditions, the symmetry conditions, and the wedge surface conditions.

Outer Boundary Conditions

A closed-boundary approach has been used to account for the upstream flux of molecules. The actual conditions which should be imposed along the outer boundaries are that at $x = \pm\infty$ and $y = \pm\infty$ the flow field recovers an equilibrium distribution function characterized by the free-stream quantities. In the past,[23,24] this space has been mapped into a compact finite region of unit dimensions. In using the method of integration along characteristic lines this approach no longer results in a set of simplified equations as those given in (2-19), (2-20), and (2-21) because the characteristic lines are now curved. Further,

the mapping transforms the wedge into a complicated shape creating difficulties in applying the surface boundary conditions. Therefore, rather than use this technique the free-stream conditions at infinity are assumed to be satisfied at locations much closer to the wedge. Yet, these boundaries are sufficiently removed so that the error introduced is negligible in the vicinity of the body. The outer boundary conditions are imposed on these new boundaries by specifying the equilibrium distribution functions of the free-stream flow, that is,

$$g_{ob} = \frac{1}{\pi} \exp \left[- (v_x - u_{x,\infty})^2 - v_y^2 \right]$$

$$h_{ob} = \frac{g_{ob}}{2}$$

Symmetry Conditions

As a consequence of obtaining the solution about a symmetric wedge, only the flow field over the upper half of the body needs to be determined. The conditions applied along the line of symmetry upstream and downstream of the wedge are that g and h for (v_k, v_ℓ) are respectively equal to g and h for $(v_k, -v_\ell)$. This condition places a restraint that the discrete velocity points in v_y must be symmetric about the line $v_y = 0$. Macroscopically, this condition establishes that u_y and the tangential stress along the center line is zero.

Surface Boundary Conditions

The molecular reflection from the surface has been assumed to be completely diffuse for this study. This is a reasonable

approximation for most aerodynamic surfaces. The assumption of diffuse reflection implies that the distribution functions of the reflected molecules are characterized by the wall temperature T_w and by the velocity of the wall relative to the coordinate system, which for this case is zero. The diffuse model requires the evaluation of a wall number density coefficient n_w. This unknown coefficient is determined by enforcing the condition that the net mass flux across the solid surface at any point is zero, thus insuring that there is no molecular build up on the surface. For the rear surface this condition is given by

$$\int_{-\infty}^{\infty}\int_{0}^{\infty} v_x g_{w,r}\, dv_x dv_y = -\int_{-\infty}^{\infty}\int_{-\infty}^{0} v_x g_{ir}\, dv_x dv_y \tag{2-22}$$

where

$$g_{w,r} = \frac{n_{w,r}}{\pi T_w} \exp\left[-\frac{1}{T_w}(v_x^2 + v_y^2)\right] \tag{2-23}$$

and for the slant surface by

$$\int_{-\infty}^{\infty}\int_{v_x \tan\alpha}^{\infty} (v_x \sin\alpha - v_y \cos\alpha) g_{w,s}\, dv_y dv_x = \tag{2-24}$$

$$-\int_{-\infty}^{\infty}\int_{-\infty}^{v_x \tan\alpha} (v_x \sin\alpha - v_y \cos\alpha) g_{is}\, dv_y dv_x$$

where

$$g_{w,s} = \frac{n_{w,s}}{\pi T_w} \exp\left[-\frac{1}{T_w}(v_x^2 + v_y^2)\right] \tag{2-25}$$

In the above equations g_{ir} and g_{is} represent the first reduced distribution functions of the incoming flux of molecules to the rear and slant surfaces of the wedge respectively.

The left-hand sides of Equations (2-22) and (2-24) are easily integrated resulting in

$$n_{w,r} = -2\sqrt{\frac{\pi}{T_w}} \int_{-\infty}^{\infty} \int_{-\infty}^{0} v_x g_{ir} dv_x dv_y \tag{2-26}$$

and

$$n_{w,s} = 2\sqrt{\frac{\pi}{T_w}} \int_{-\infty}^{\infty} \int_{-\infty}^{v_x \tan \alpha} (v_x \sin \alpha - v_y \cos \alpha) g_{is} dv_y dv_x \tag{2-27}$$

The distribution functions g_{ir} and g_{is} are not known a priori; consequently, the wall number density coefficients can be determined only after first evaluating the distribution functions for those characteristic lines which terminate at the solid surfaces (i.e., g_{ir} and g_{is}).

CHAPTER III

NUMERICAL METHODS OF SOLUTION

Solution of the Equations

As stated previously, Equations (2-20) and (2-21) are the equations which must be solved in conjunction with the characteristic equation (2-19). Since the reduced Boltzmann equations are of the same form, only the solution of (2-19) and (2-20) will be considered; the other follows in a similar manner. Thus the equations to be solved are:

$$\left(\frac{dy}{dx}\right)_{char} = \frac{v_\ell}{v_k}$$

and

$$v_k \frac{dg_{k,\ell}}{dx} = \nu(G_{k,\ell} - g_{k,\ell})$$

A gridwork is established around the wedge and a solution to the above equations is sought at the points of intersection of the grid lines with themselves or with the solid surfaces of the wedge.

Equation (2-20) can be arranged in the form

$$dg_{k,\ell} = \frac{\nu}{v_k}(G_{k,\ell} - g_{k,\ell})dx \qquad (3\text{-}1)$$

At this point an integrating factor could be introduced, with the result that $g_{k,\ell}$ is given by

$$g_{k,\ell}(x) = \exp\left[-\int_{x_a}^{x} \frac{\nu(t)}{v_k}\,dt\right] \times$$

$$\left\{\int_{x_a}^{x} \frac{\nu(t)}{v_k}\, G_{k,\ell}(t)\, \exp\left[\int_{x_a}^{t} \frac{\nu(\theta)}{v_k}\,d\theta\right]dt + g_{k,\ell}(x_a)\right\}$$

Here x_a is a location where $g_{k,\ell}$ is known; e.g., the outer boundaries. The integrals which are required are rather complicated to evaluate numerically and a simpler approach has been taken. Both sides of Equation (3-1) are integrated and for convenience the subscripts k and ℓ are dropped.

$$g(x) - g(x_a) = \int_{x_a}^{x} \frac{\nu}{v_k}\,(G - g)\,dx \tag{3-2}$$

Since the functional relationship of the remaining integral is unknown, it has been replaced by the linear approximation

$$\int_{x_a}^{x} \frac{\nu}{v_k}\,(G - g)\,dx \doteq \tag{3-3}$$

$$\left\{\frac{\nu(x)[G(x) - g(x)] + \nu(x_a)[G(x_a) - g(x_a)]}{2}\right\} \frac{x - x_a}{v_k}$$

This is a trapezoidal integration spanning the distance from x_a to x. This results in

$$g - g_a = \left[\frac{\nu(G - g) + \nu_a(G_a - g_a)}{2}\right] \frac{x - x_a}{v_k} \tag{3-4}$$

where

$$g_a = g(x_a)$$

$$G_a = G(x_a)$$

and

$$\nu_a = \nu(x_a)$$

Rearranging the terms gives

$$g = \frac{g_a + \left[\frac{\nu_a(G_a - g_a) + \nu G}{2}\right] \frac{x - x_a}{\nu_k}}{1 + \frac{\nu(x - x_a)}{2\nu_k}} \tag{3-5}$$

Since the scheme is based on a linear approximation, the results obtained are most accurate if the difference between x and x_a is kept small when the rate of change in the gradient of g is large. It may be increased as g tends toward a constant value. Consequently, the value of x_a must be constantly changed as the integration moves along the characteristic line. This is made possible by establishing the values of g at the grid points one step inward and then interpolating the values at a new x_a using these previously developed values. An example can best demonstrate this process. Figure 3 shows a typical gridwork. The characteristic line is denoted by β and the slope is ν_ℓ/ν_k. In the example, $\nu_k < 0$ and $\nu_\ell < 0$. The object is to determine g at (x_i, y_j) knowing all properties at (x_i, y_{j+1}) and (x_{i+1}, y_{j+1}). These values are known either as a consequence of the points being on a

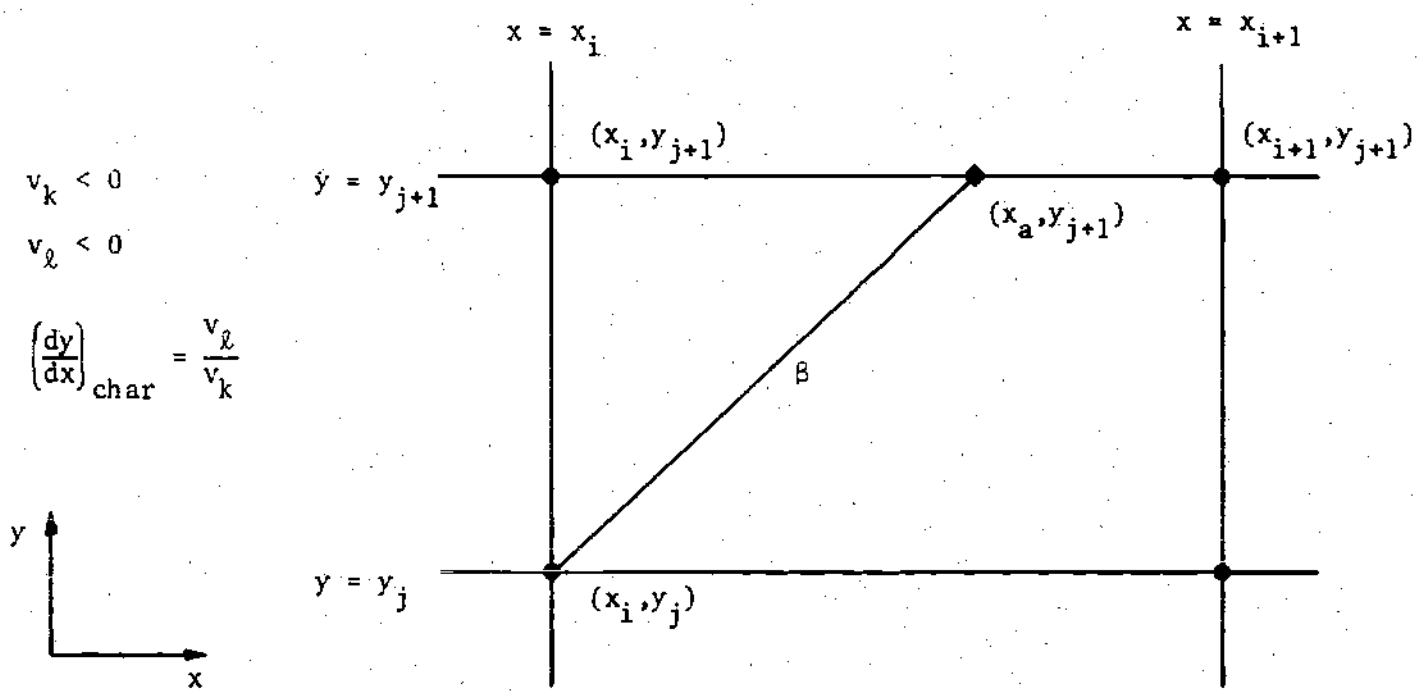

Figure 3. A Grid System with a Related Characteristic Line

boundary or having been previously determined. $G(x_i,y_j)$ and $\nu(x_i,y_j)$ are assumed to be known as the result of an initial guess of the macroscopic properties. This point will be discussed later. The characteristic line passes through (x_i,y_j) and crosses the grid line joining the points (x_i,y_{j+1}) and (x_{i+1},y_{j+1}) at the point (x_a,y_{j+1}). This is the value of x_a at which the integration given in Equation (3-5) is assumed to begin. Since the properties are known only at (x_i,y_{j+1}) and (x_{i+1},y_{j+1}) a suitable interpolation must be used to obtain their values at x_a. To maintain the consistency of the scheme, a linear interpolation is used. If θ is any property, then $\theta(x_a,y_{j+1})$ is given by

$$\theta_{a,j+1} = \theta_{i,j+1} + \left[\frac{\theta_{i+1,j+1} - \theta_{i,j+1}}{x_{i+1} - x_i}\right](x_a - x_i) \tag{3-6}$$

where

$$\theta_{p,q} = \theta(x_p,y_q)$$

The difference $x_a - x_i$ is obtained by integrating the characteristic Equation (2-19) from x_a to x_i. This yields

$$x_a - x_i = \frac{v_k}{v_\ell}(y_{j+1} - y_j) \tag{3-7}$$

Upon substituting (3-7) into (3-6), $\theta_{a,j+1}$ is given by

$$\theta_{a,j+1} = \theta_{i,j+1}\left[1 - \frac{v_k}{v_\ell}\frac{y_{j+1} - y_j}{x_{i+1} - x_i}\right]$$

$$+ \theta_{i+1,j+1}\left[\frac{v_k}{v_\ell}\frac{y_{j+1} - y_j}{x_{i+1} - x_i}\right]$$

Thus the unknown properties at x_a can be calculated. Upon using this technique in Equation (3-5) where $x = x_i$, and $g = g_{k,\ell}(x_i,y_j)$, g is determined. A similar process is carried out for the remaining characteristic lines with the result that $g_{k,\ell}(x_i,y_j)$ is evaluated for all the discrete velocity points, thus providing the necessary information to obtain the macroscopic properties.

Macroscopic Properties

The nondimensional macroscopic properties are determined by numerically evaluating the nondimensionalized forms of the integrals found in Equations (2-13) through (2-16). These integrals can be expressed in a general form given by

$$P(x,y) = \int_{-\infty}^{\infty}\int_{-\infty}^{\infty} \Phi(v_x,v_y)\Lambda(g,h)dv_x dv_y$$

where

$$g = g(x,y,v_x,v_y)$$

and

$$h = h(x,y,v_x,v_y)$$

Φ is a function solely of v_x and v_y which, when associated with Λ, a functional of g and h, and integrated as indicated above, results in the physical property P.

A finite double summation is used to approximate the double integration for P; that is,

$$P(x,y) = \sum_{k=1}^{k_e} \sum_{\ell=1}^{\ell_e} w_k w_\ell \Phi(v_k, v_\ell) \Lambda(g_{k,\ell}, h_{k,\ell})$$

where

$$g_{k,\ell} = g(x,y;v_k,v_\ell)$$

$$h_{k,\ell} = h(x,y;v_k,v_\ell)$$

and w_i is the appropriate weight for the function evaluated at the corresponding v_i. As mentioned in Appendix A, the discrete ordinates have been taken to be the quadrature points for this process and hence the results are obtained immediately by performing the double summation described above.

Incorporation of the Boundary Conditions

The inclusion of the outer boundary conditions and symmetry conditions are straightforward. The surface boundary conditions are more complicated and for the slant surface require special numerical techniques. The rear and slant surface wall number density coefficients must be obtained before a characteristic line can originate from any point on either of these surfaces. This imposes a restriction that characteristic lines crossing any surface point and originating from the flow field must be solved first, so that the condition of zero mass flux across the surface may be applied to find n_w. After taking this into account, these coefficients are obtained by performing the remaining integrations in Equations (2-26) and (2-27). These integrations must be implemented using the tabulated values of g_{ir} and g_{is}. The

integration for $n_{w,r}$ is simplified by choosing the discrete ordinate points and their associated weights as described in Appendix A, such that the quadrature points do not span $v_x = 0$; that is, the interval on v_x from $-\infty$ to ∞ is divided into two intervals, one from $-\infty$ to 0 and the other from 0 to ∞. Then, $n_{w,r}$ is given by

$$n_{w,r} = -2\sqrt{\frac{\pi}{T_w}} \sum_{k=1}^{k_0^-} \sum_{\ell=1}^{\ell_e} w_k w_\ell v_k (g_{k,\ell})_{ir} \tag{3-9}$$

The slant surface number density coefficient is complicated by the variable upper limit in the integral along v_y

$$n_{w,s} = 2\sqrt{\frac{\pi}{T_w}} \int_{-\infty}^{\infty} \int_{-\infty}^{v_x \tan \alpha} (v_x \sin \alpha - v_y \cos \alpha) g_{is} dv_y dv_x$$

The problem is simplified by splitting the integral into three parts.

$$\int_{-\infty}^{\infty} \int_{-\infty}^{v_x \tan \alpha} v_n g_{is} dv_y dv_x = \int_{-\infty}^{0} \int_{-\infty}^{v_x \tan \alpha} v_n g_{is} dv_y dv_x \tag{3-10}$$

$$+ \int_{0}^{\infty} \int_{-\infty}^{0} v_n g_{is} dv_y dv_x$$

$$+ \int_{0}^{\infty} \int_{0}^{v_x \tan \alpha} v_n g_{is} dv_y dv_x$$

where

$$v_n = v_x \sin \alpha - v_y \cos \alpha$$

It is interesting to note that each integral represents the flux of molecules normal to the surface from one quadrant.

Due to the fact that no variables appear in the limits of integration in the second integral, it is evaluated in a straightforward manner similar to the determination of the rear surface wall number density coefficients. The approximations to the two remaining integrals follow in a similar manner; hence, only the first will be considered. The first integral can be represented as

$$\int_{-\infty}^{0} \int_{-\infty}^{v_x \tan \alpha} v_n g_{is} dv_y dv_x = \int_{-\infty}^{0} \Psi(v_x) dv_x$$

where

$$\Psi(v_x) = \int_{-\infty}^{v_x \tan \alpha} v_n g_{is} dv_y$$

The quadrature developed for the discrete ordinate method is applied to this integral giving

$$\int_{-\infty}^{0} \Psi(v_x) dv_x = \sum_{k=1}^{k_0} w_k \Psi(v_k)$$

But

$$\Psi(v_k) = \int_{-\infty}^{v_k \tan \alpha} v_{n,k} (g_k)_{is} dv_y$$

where

$$v_{n,k} = v_k \sin \alpha - v_y \cos \alpha$$

Therefore

$$\int_{-\infty}^{0}\int_{-\infty}^{v_x \tan\alpha} v_n g_{is}\, dv_y dv_x = \sum_{k=1}^{k_0^-} w_k \int_{-\infty}^{v_k \tan\alpha} v_{n,k}(g_k)_{is}\, dv_y \qquad (3\text{-}11)$$

The problem has now been reduced to evaluating the inner integral. To do this $g_{k,\ell}$ is tabulated at the surface for each specific v_k, and all v_ℓ's such that $-\infty < v_\ell < v_k \tan\alpha$. A curve is fitted through the tabulated points and is then integrated using the Romberg integration technique.[26]

Finally, $n_{w,s}$ is given by

$$n_{w,s} = 2\sqrt{\frac{\pi}{T_w}}\left[\sum_{k=1}^{k_0^-} w_k \int_{-\infty}^{v_k \tan\alpha} (v_k \sin\alpha - v_y \cos\alpha)(g_k)_{is}\, dv_y \right. \qquad (3\text{-}12)$$

$$+ \sum_{k=k_{0^+}}^{k_e} \sum_{\ell=1}^{\ell_0^-} w_k w_\ell (v_k \sin\alpha - v_\ell \cos\alpha)(g_{k,\ell})_{is}$$

$$\left. + \sum_{k=k_{0^+}}^{k_e} w_k \int_{0}^{v_k \tan\alpha} (v_k \sin\alpha - v_y \cos\alpha)(g_k)_{is}\, dv_y \right]$$

Overall Method

As a consequence of using the BGK model ν, G, and H must be known a priori in order to determine g and h. However, ν, G, and H depend on the local macroscopic properties, which are unknown and are, in fact, being sought. To overcome this lack of information a Picard iteration scheme[27,28] is now applied to the overall problem. An

initial guess is made of the macroscopic properties. If the computed set is the same as the initial one, then the guess was the correct solution. Generally, this is not the case. The new set of properties is assumed to be a better approximation to the actual solution and is used to recompute ν, G, and H from which another set of macroscopic properties is obtained. Convergence of the solution is obtained by continuing this process until the difference between macroscopic properties for successive iterations becomes acceptably small.

Convergence and Stability of the Numerical Scheme

A simple test was designed to examine the stability and convergence of the iterative scheme. Before attempting a numerical solution for the complete problem of a wedge in a hypersonic flow, it was deemed advisable to test, inasmuch as possible, the stability and convergence of the scheme for a much simpler problem. A sample case was devised in which the wedge was made "transparent" to the flow; that is, the boundary conditions at the wedge surface were specified such that the body creates no disturbance to the oncoming flow. Thus, if the numerical scheme behaves properly, the flow field about the wedge should recover to the uniform free stream if perturbed by some artificial means. Figure 4 depicts the flow field with its associated grid network. The points indicated are those at which one physical property was disturbed from its free-stream value. The numerical technique was then allowed to iterate on this perturbed flow field. It was observed that the flow field in the proximity of the perturbation was only slightly affected by the disturbances, indicating that the scheme was stable. After four iterations the solution had returned to that of a

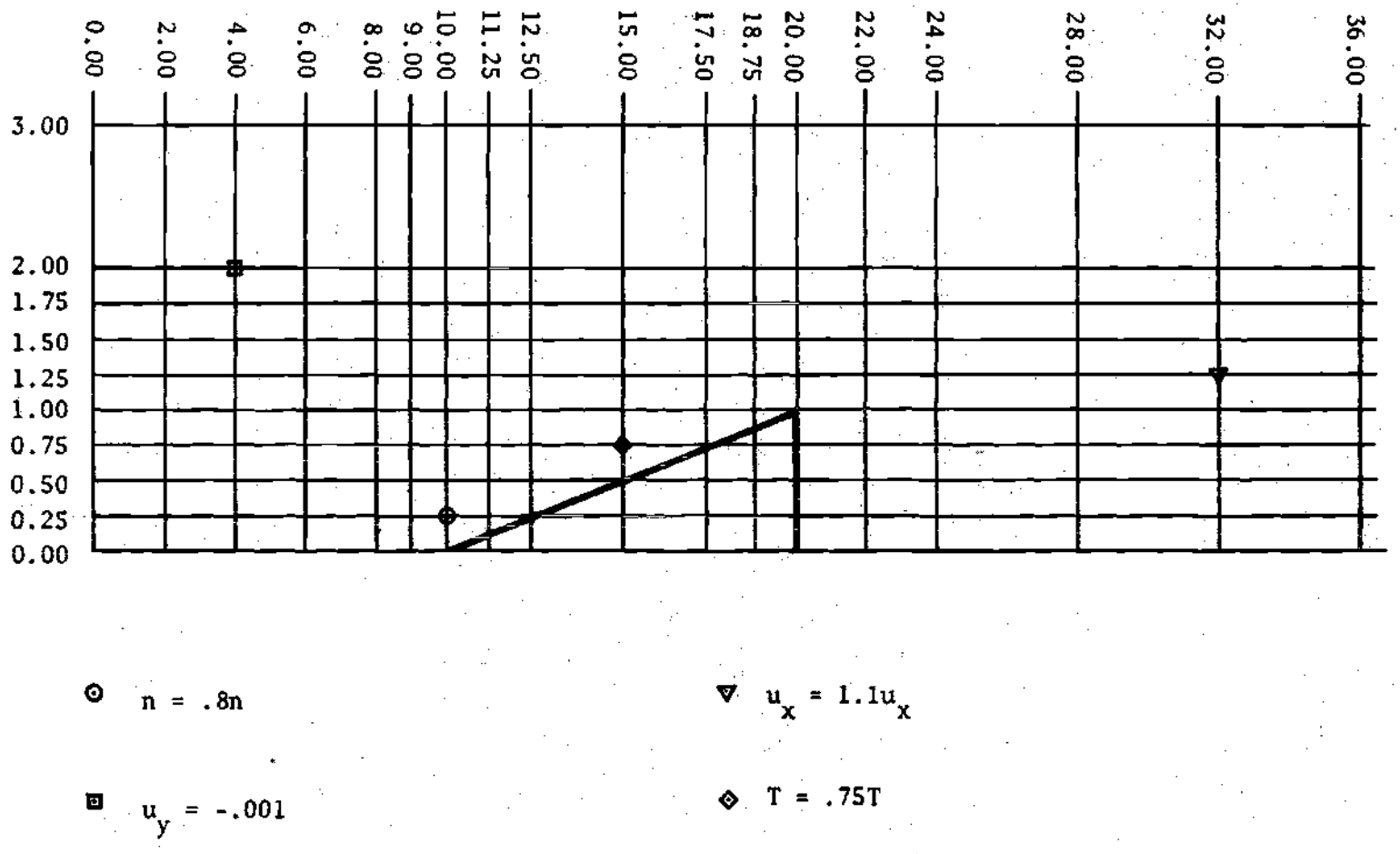

Figure 4. Hypersonic Flow Field About a "Transparent" Wedge

uniform flow, indicating convergence.

One important aspect of the numerical scheme was revealed in this test. Although only one physical property was perturbed at each of the points, and the remaining grid nodes were kept initially at the exact solution, the method required four iterations to return to the correct value. This shows that the scheme tends to be somewhat slow in converging; but an accuracy of better than 0.2 percent was obtained after four iterations. The slow convergence is a consequence of the first order integration and interpolation techniques employed to maintain an ease in computation and to keep the program within limitation of the available computer system. The stability of the numerical system was further demonstrated as an actual solution was being obtained. In the real problem, trends in the flow properties became apparent as the iterations progressed, and an attempt was made to speed up convergence by applying extrapolation to a physical property. The property which was chosen was the wall number density coefficient used in the reflection model. These densities were changed to reflect an acceleration of approximately five iterations. Upon allowing the scheme to iterate on the new conditions no noticeable change occurred in the convergence of this property. In fact, the number densities immediately reverted to about the expected value for two iterations after the change. This phenomena seems to indicate an inherent stability in the scheme, but with a rather slow convergence.

Accuracy of the Numerical Scheme

The limits of accuracy of a numerical scheme as complicated as this are difficult to establish precisely. The accuracy is dependent

on such a wide range of parameters that the singling out of any particular one as being responsible for any errors is almost impossible. However, factors which certainly affect accuracy include: computer round off and truncation errors, the accuracy of the numerical approximations, and the relative distance from the wedge to the outer boundaries. In addition to numerical accuracy, there are inherent approximations in employing the BGK model as a replacement for the full collision integral in the Boltzmann equation.

To obtain some idea of the overall accuracy of the scheme an algorithm was developed to check the conservation of mass within a control volume surrounding the wedge. The algorithm evaluates the mass flux entering and leaving the volume, utilizing a trapezoidal integration. The results should be that net mass influx is equal to the efflux. Generally, this is not the case, the discrepancy being the result of two simultaneous inaccuracies. The first is a result of the trapezoidal integration, which goes as the square of the distances between the points and was used because of the uneven spacing of the grid. This error is not related to that of the numerical solution of the integro-differential equation. The second is due to the actual error in the solution of the Boltzmann equation. It should be noted that for the high velocities associated with hypersonic flow, a small discrepancy in density might produce a relatively large change in the total mass flow, and as a consequence the error of specific points may be less than that of the whole field. Since the errors of this algorithm cannot be separated from each other, it is assumed that if the combined error is small, then it is small for each of them.

CHAPTER IV

RESULTS

Flow Field Specifications

The numerical processes described in the previous chapter were incorporated into a FORTRAN program. A solution has been obtained using this program for a wedge of length 45 λ_∞ and half-angle 6.026°. The free-stream Mach number is 6 and the wedge surface temperature is $0.42T_o$, where T_o is the free-stream stagnation temperature. This results in a ratio of 5.46 between the body temperature and the free-stream static temperature. The gas was assumed to be argon and the exponent for the power law, used to determine the viscosity coefficient, is taken to be 0.816 as given in Reference 29. The leading edge of the wedge is located at x = 20.00 and the boundaries of the flow were placed at x = 0.00, x = 185.00, y = 0.00, and y = 70.00. The grid network chosen contains 1623 grid points. The spacing varied from 0.475 λ_∞ in the vicinity of the surfaces to 20 λ_∞ in the wake region behind the wedge. Tables for the grid lines used are given in Appendix C.

A set of second order Gaussian quadratures was used to calculate the moment integrations. Since the quadratures were not capable of spanning the infinite domain, an approximation was made: the v_x limits were located at 10 and -7 and the limits for v_y at 7 and -7. The choice of length for the subintervals of the quadratures resulted in 44 discrete v_x points and 48 v_y points. These points were accurate in recovering the macroscopic properties, in the free-stream limit, to

within .03 percent of their exact values.

Under these conditions each iteration took, on the average, about 30 CPU minutes to run on the UNIVAC 1108 located on the Georgia Institute of Technology campus. Satisfactory convergence for the flow field of interest was reached after 45 iterations. To aid in debugging the program, free-stream conditions were taken as the initial approximation. A better choice of the initial guess would probably produce an accelerated convergence.

The conservation of mass algorithm described previously gave a maximum error of 8 percent for the control volumes examined. For control volumes whose boundaries were in the neighborhood of the wedge, the errors were as small as 3.5 percent. It is emphasized that these errors are composed of two parts: that due to the trapezoidal integration scheme used to determine the fluxes and that arising as numerical error in the solution of the integro-differential equation.

Macroscopic Property Profiles

The theoretical approach taken in this dissertation requires no *a priori* assumptions of the existence of specific zones or regions in the flow since the entire field is calculated from a single governing equation. However, for explanatory purposes the flow may be considered as a merged composite of a thick shock, a viscous surface layer, an essentially inviscid compression, and a wake, all interacting with each other in varying degrees in different physical regions. This type of breakdown into the continuum limit regimes is useful in understanding and discussing the basic behavior of the flow. However, in interpreting the finer details, emphasis must be placed on the molecular aspects of

the gas. Particular consideration must be given to the general non-equilibrium state of the flow as well as the length scale of the field, which is several orders of magnitude smaller than is commonly encountered in continuum studies.

The flow field results for number density, velocity components, and temperature are plotted for several x-stations in Figures 5 through 17. To avoid a large number of plots in any figure, the number of x-locations have been divided into three regions. Profiles for each macroscopic property are plotted for these various x-stations. In most of the graphs, the plots extend from y = 0.00 (i.e., center line) to y = 30.00. In the region where the shock extends above 30 λ_∞ the data obtained for those points closer to the outer boundary may be suspected of having a greater error since only four grid points separate y = 70.00 from y = 30.00. It will also be noted that the trailing edge station does not appear in any of the plots. This point, where the slant surface and rear surface join, represents a double point in the flow for a mathematically ideal wedge. Consequently, it has been omitted from the plots. Furthermore, it should be reemphasized that the x-axis lies along the center line of the wedge rather than along the slant surface. Consequently, profiles which contain a surface point will not begin at y = 0 except at the leading edge.

Number Density

The number density profiles are given in Figures 5 through 8. Figure 5 depicts the properties near the leading edge. At x = 13.00 (i.e., 7 λ_∞ ahead of the leading edge), n is barely affected by the presence of the wedge, whereas at x = 18.00 the density shows a clear

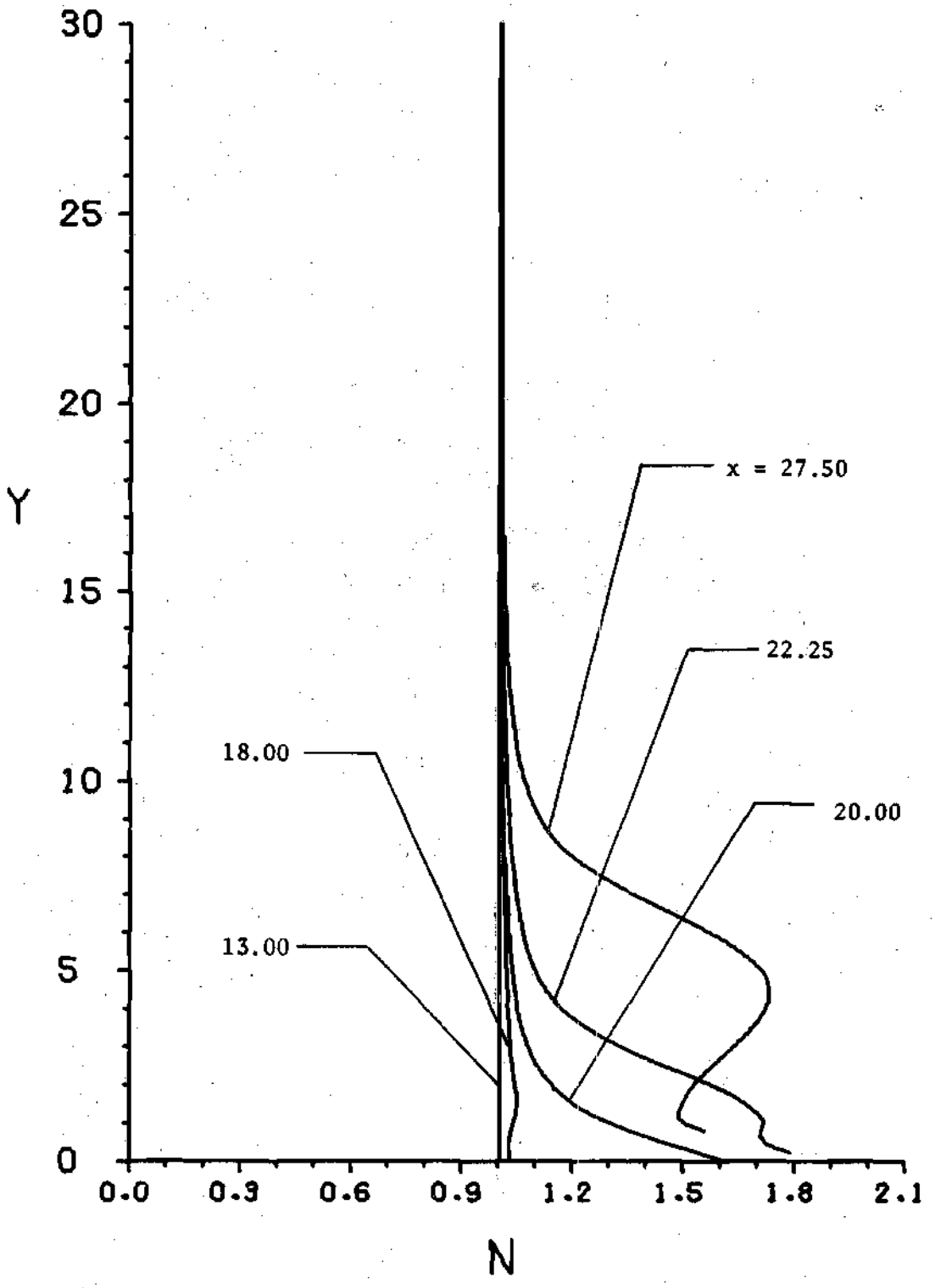

Figure 5. Number Density, x < 33.50

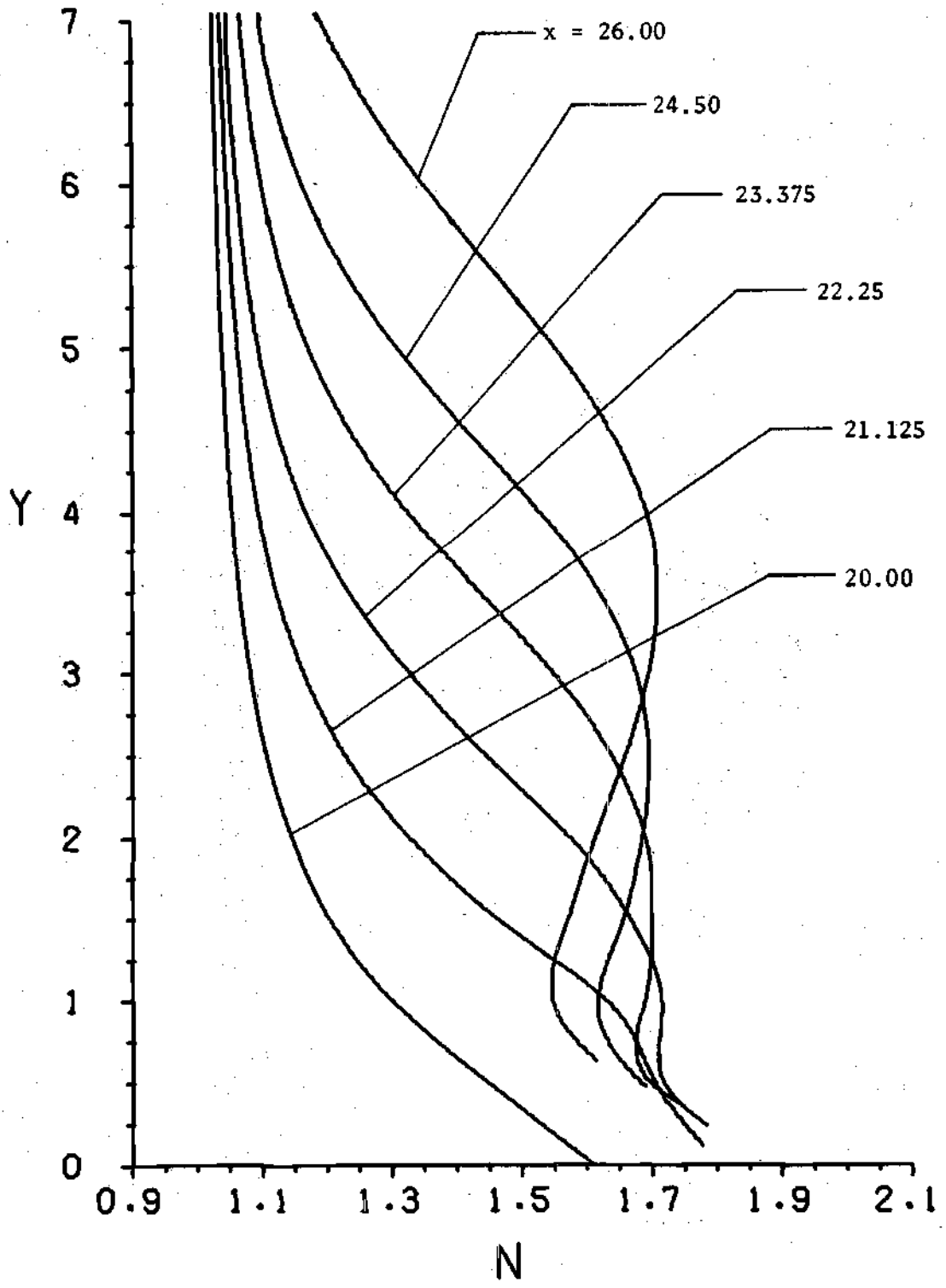

Figure 6. Number Density in the Vicinity of the Leading Edge

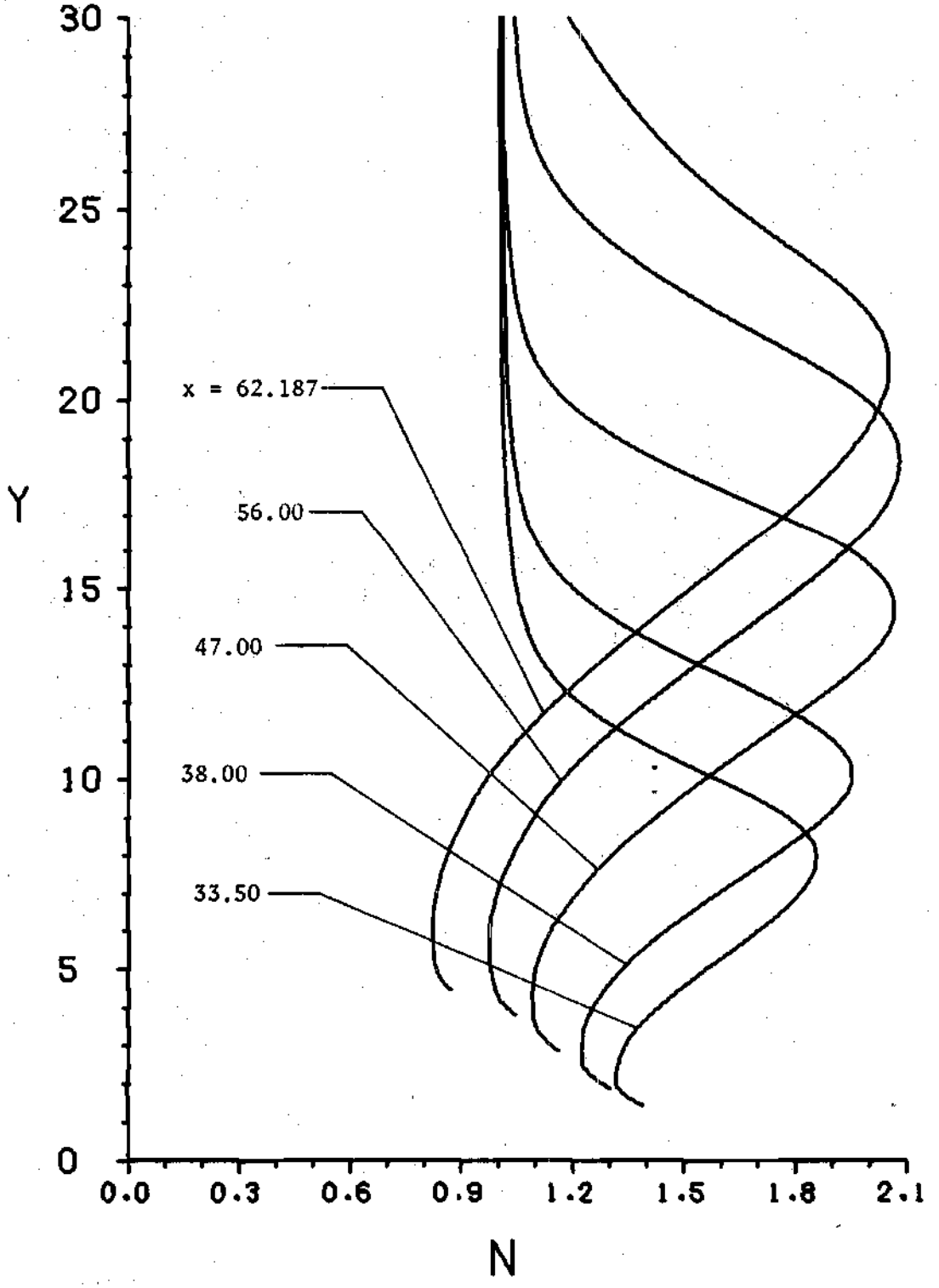

Figure 7. Number Density, $33.50 \leq x < 64.437$

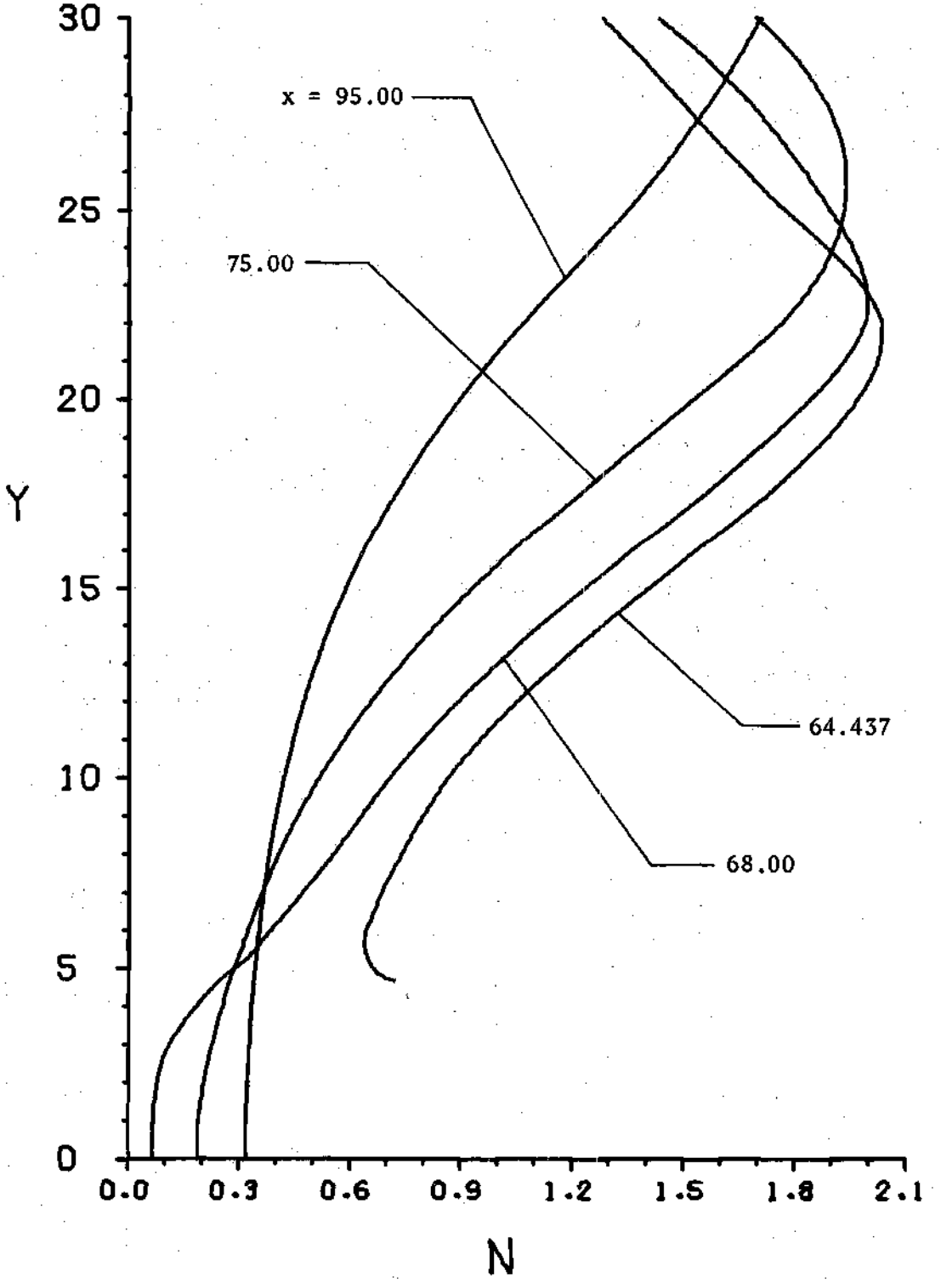

Figure 8. Number Density, $x \geq 64.437$

deviation from the free-stream value. This is due to the effect of the upstream flux of molecules communicating the presence of the solid body to the oncoming flow. At the leading edge (x = 20.00), the number density increases markedly at the surface as a result of molecular collisions with the body. The surface value exceeds the free molecular flow value of 1.29. The density rapidly decreases with distance from the body and asymptotically approaches 1.00.

At x = 22.25 the number density on the surface has further increased, and the emergence of a shock-like structure is becoming evident. In moving toward the surface at $y \simeq 1$ the characteristic increase in density associated with a shock is present after which a layer, dominated by viscosity and the proximity of the surface, appears immediately. A considerable portion of these two phenomena are obviously merged. Proceeding in the x-direction, the shock and viscous surface layer become more distinctly apparent. The formation and separation of these regions are presented in greater detail in Figure 6. The shock development is quite evident at x = 26.00 and continues to grow in strength becoming the dominant feature of the profiles (see Figure 7). The nature of flow is that of the merged layer regime in which the shock thickness is comparable to the height of the the disturbed flow. Further, velocity slip and temperature jump exist at the wall.

From x = 27.50 to x = 64.437 the density profiles near the surface are seen to first decrease, then increase while moving away from the surface. This decrease in number density is apparently associated with a viscous heating phenomena. As the shear stress heats the gas near the surface, the temperature rises while pressure variations in

the embryonic boundary-layer are moderate. Consequently, the number density decreases. The increase in density which follows, results from the flow accommodating to the large density rise across the shock. At x = 62.187, the effects of the wake are becoming apparent, as indicated by the decrease in the shock strength. This again is a result of the upstream influence of the molecules. Figure 8 indicates that the shock strength is further reduced at x = 64.437 and a marked density decrease occurs near the surface due to the wake. The first station plotted in the wake is at x = 68.00. Here the density is quite low for y less than 4.75, and rises rapidly in moving away from the center line, finally taking on a shock-like profile. Further downstream, a slow return to the free-stream density is seen to take place. The densities of the shock region decrease and the densities near the center line increase.

X-Velocity Component

The x-velocity profiles are plotted in Figures 9, 10, and 11. A behavior similar to that of the number density occurs ahead of the leading edge. At x = 13.00, there is little influence of the wedge, whereas at x = 18.00, the effect is obvious. For stations from x = 20.00 to x = 62.187, that is, from the leading edge to near the trailing edge, the profiles have the same basic shape. The flow tends to accommodate from the free-stream value of 5.48 to a zero velocity at the wedge surface. However, the accommodation is never completed. Although the profiles indicate that the surface velocity decreases from the leading edge to x = 56.00, nowhere does the value reach zero, the continuum, no-slip condition. At x = 56.00 a slight increase occurs as the flow begins to adjust to the expansion which is to take place over the

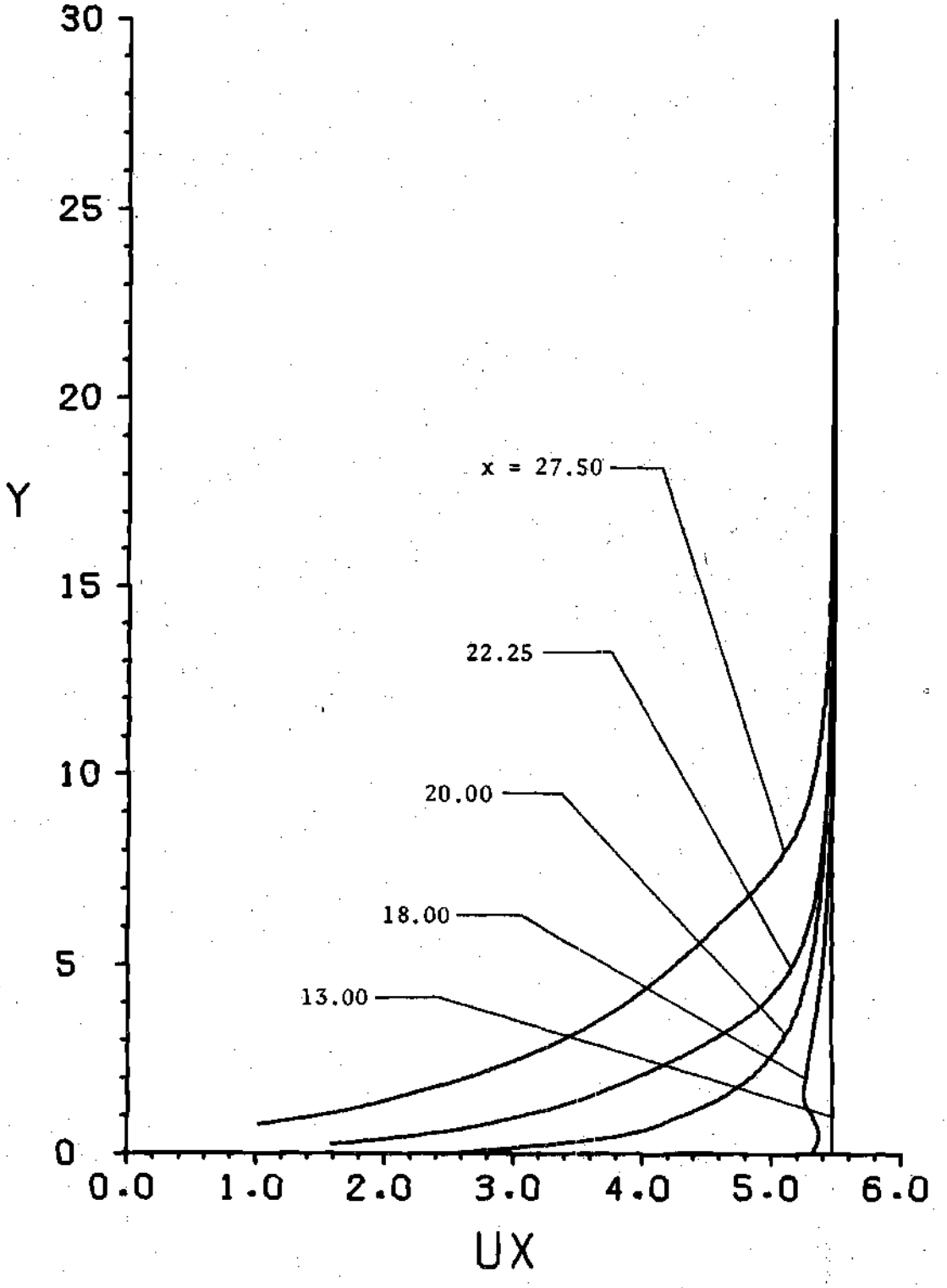

Figure 9. X-Velocity, x < 33.50

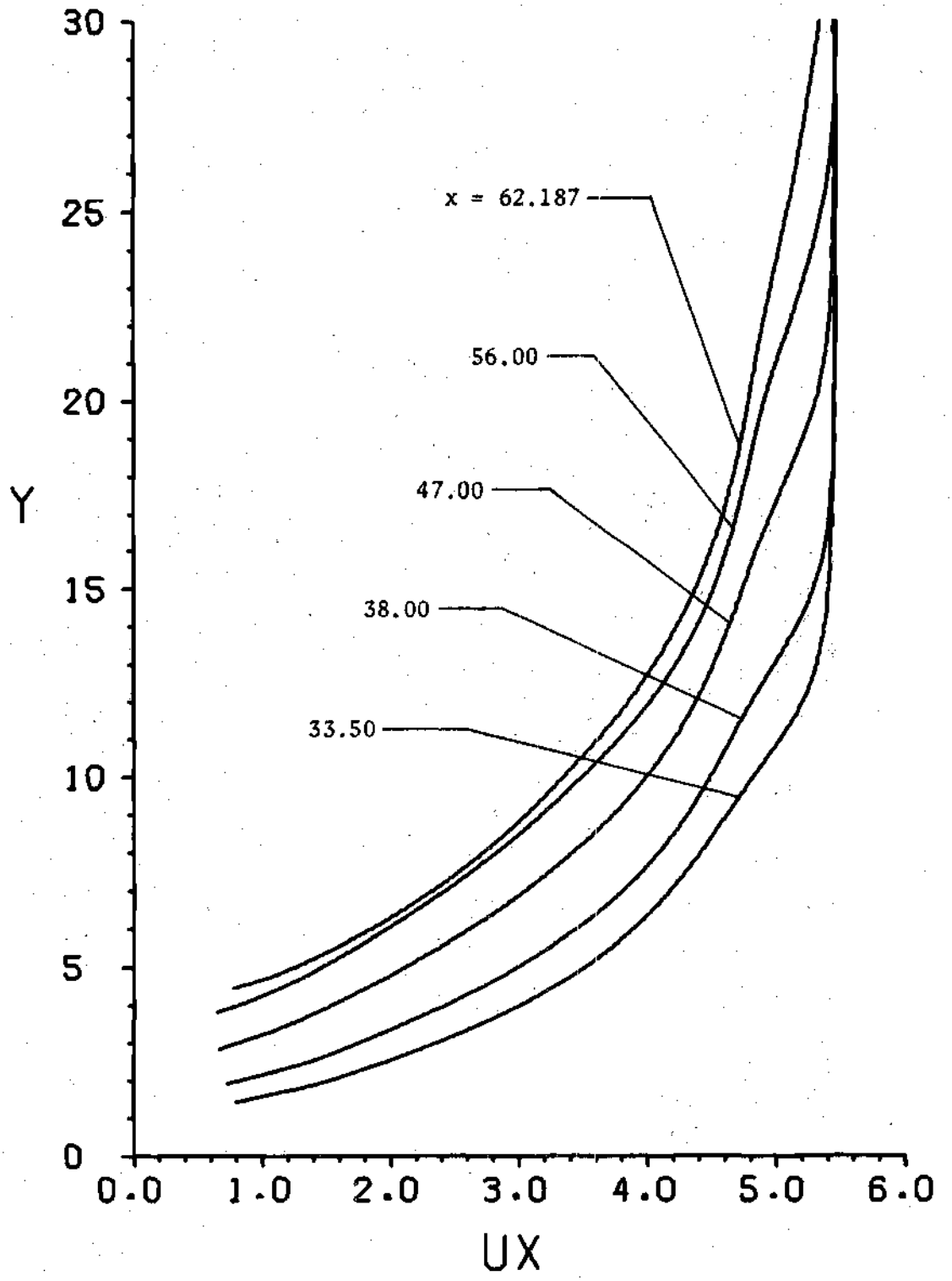

Figure 10. X-Velocity, 33.50 $\leq$ x < 64.437

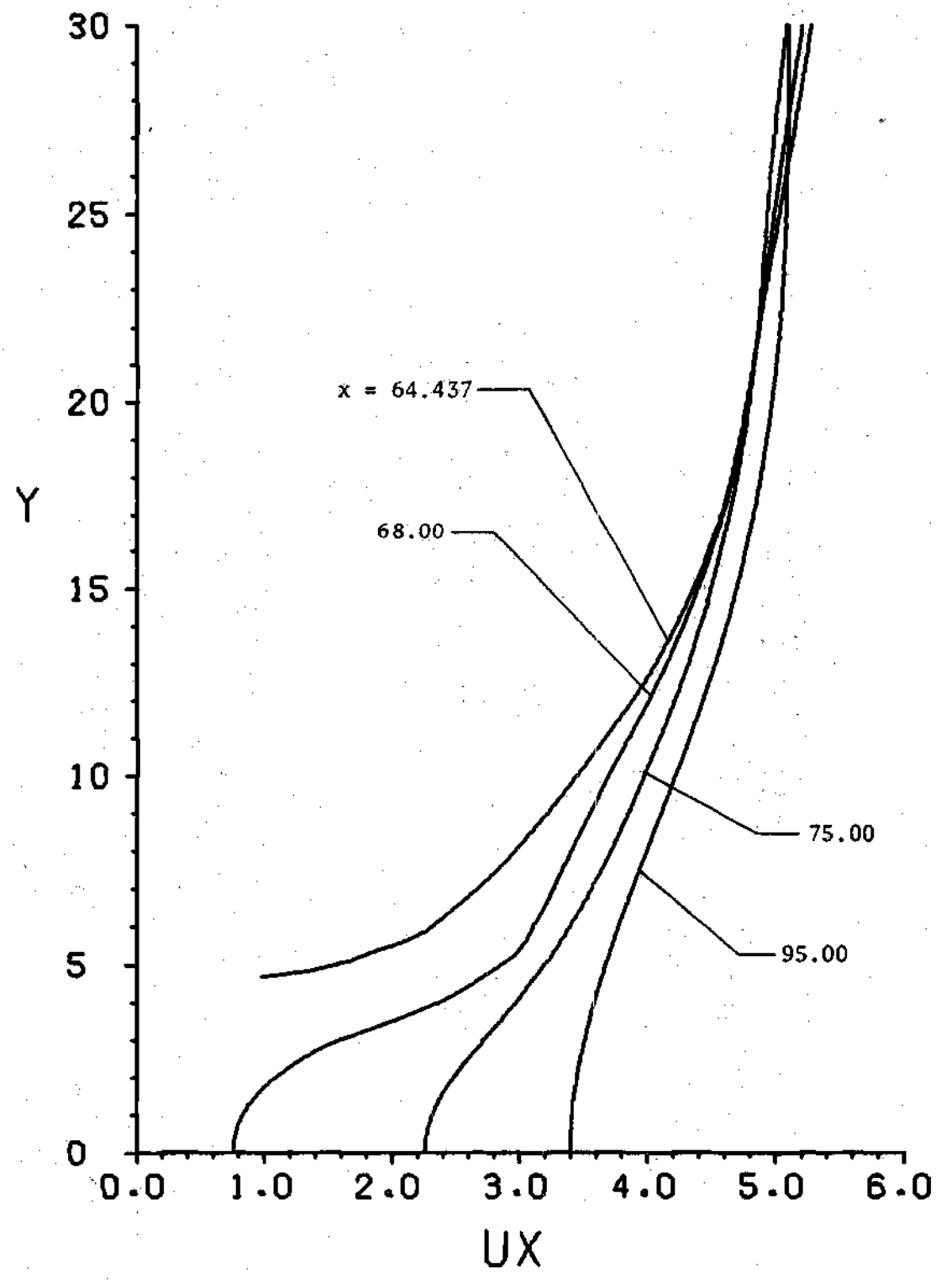

Figure 11. X-Velocity, $x \geq 64.437$

trailing edge.

In the profiles beginning at x = 33.50, there are noticeable inflections in the profiles beyond which the flow returns to a near free-stream velocity. This phenomena is the result of making observations through the shock in the y-direction rather than normal to it. The general location of these occurrences corresponds closely with the peak values in the number density profiles. At x = 64.437 the influence of the expansion and wake is clear. The profile shows a slight increase on the surface, from the previous station, followed by a rapid rise just above the body. The flow velocity increases as the gas tends to fill the low density region behind the wedge. In the wake the large velocity deficit near the base decreases with distance from the rear surface.

Y-Velocity Component

Figures 12, 13, and 14 illustrate the u_y profiles. As in the previous two properties, the effect of the solid boundary is noticed only for the first profile ahead of the leading edge. The same general shape is observed for the profiles from x = 20.00 to x = 62.187. Moving downward toward the surface from the free-stream limit, the velocity increases as a result of compression causing the flow to turn (i.e., the streamlines become inclined) as it adjusts to the surface. Further, it is evident that this velocity component also exhibits a velocity slip everywhere along the slant surface. In the case of all the profiles except the one at x = 20.00, the compression above the surface is associated with the shock or its initial formation. This can be easily seen by examining the other properties; principally, the number

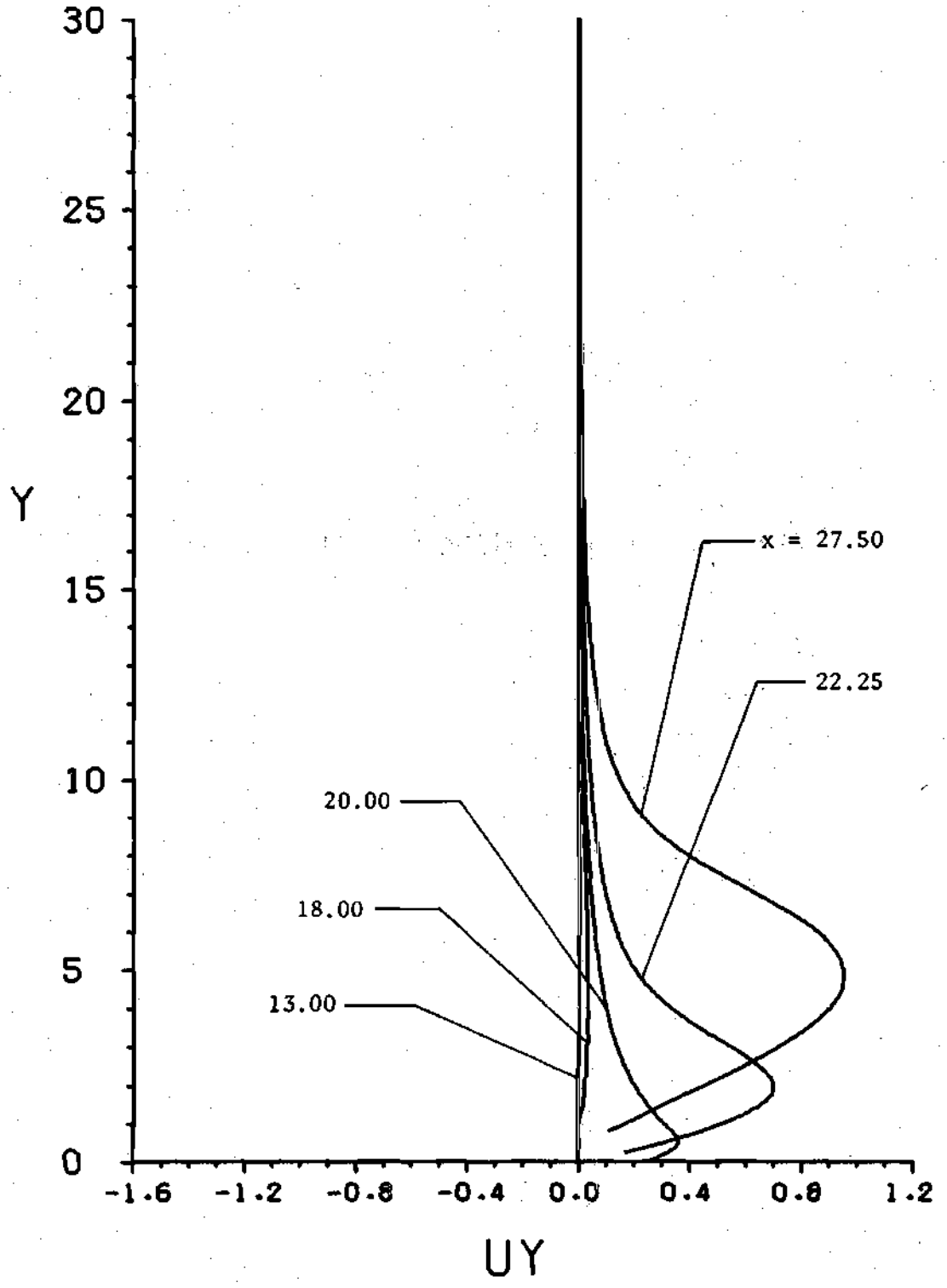

Figure 12. Y-Velocity, x < 33.50

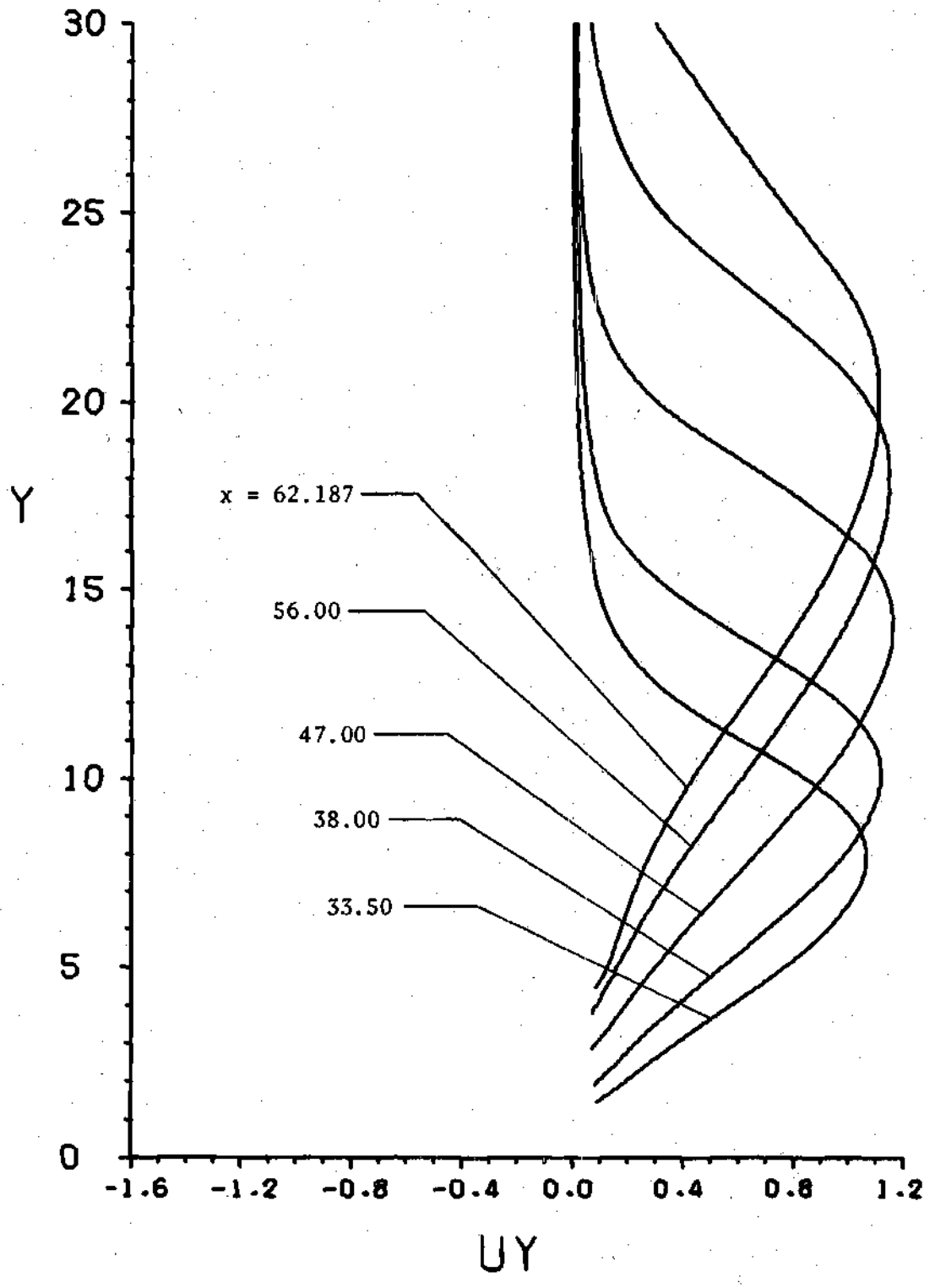

Figure 13. Y-Velocity, $33.50 \leq x < 64.437$

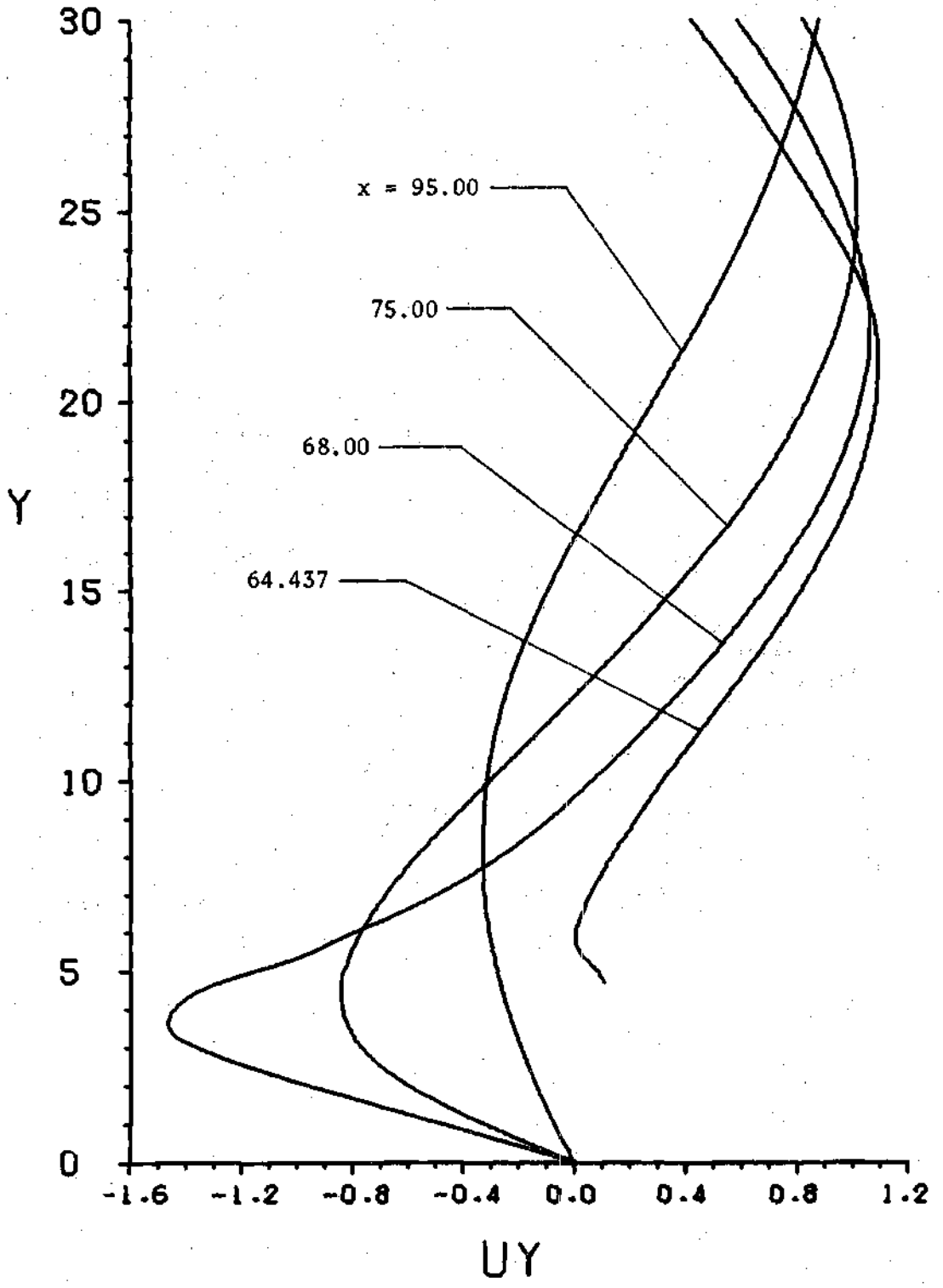

Figure 14. Y-Velocity, $x \geq 64.437$

density. For the leading edge, only u_y exhibits a shock-like compression. This illustrates the sensitivity of the y-velocity component as an indicator of shock formation. The extent of this sensitivity is more obvious if one considers the shock formation at the x-station 22.25. Of the three properties other than u_y, only in the number density profile can the shock be detected, and even for this property the disturbance is small. On the other hand the u_y profile indicates a rapid increase in velocity as the shock is approached.

At x = 56.00 the effects of the wake can be detected in that there is a slight decrease in the maximum velocity. Once again, at x = 62.187 the effect becomes obvious. The surface velocity begins to increase and the character of the profile changes slightly. At the next plotted station, near the surface, the profile has changed dramatically. Just above the body the velocity decreases as the gas begins to adjust to the rapid expansion downstream. At a distance further from the surface, the velocity increases in accommodating to the deflection caused by the weakened shock. The y-component of velocity becomes negative in the wake as is expected. The negative portion propagates further upward into the flow and the magnitudes decrease in moving away from the rear of the wedge.

Temperature

The plots of the gas temperature profiles are found in Figures 15 through 17. The effects of the leading edge are observed farther upstream for this property. At x = 13.00, the profile deviates by as much as 15 percent over the free-stream temperature and at x = 18.00, near the center line, the temperature is doubled. This implies that

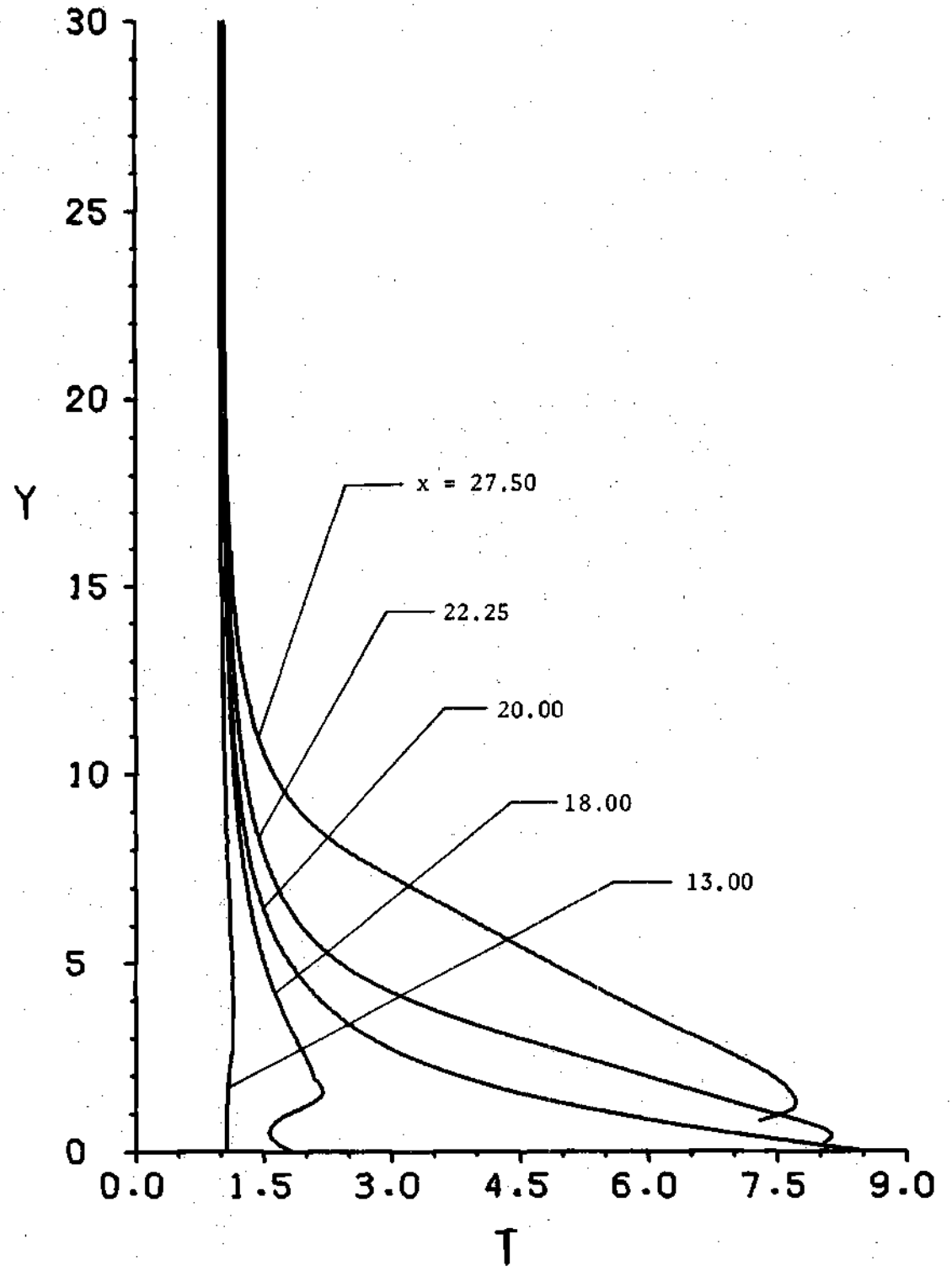

Figure 15. Temperature, x < 33.50

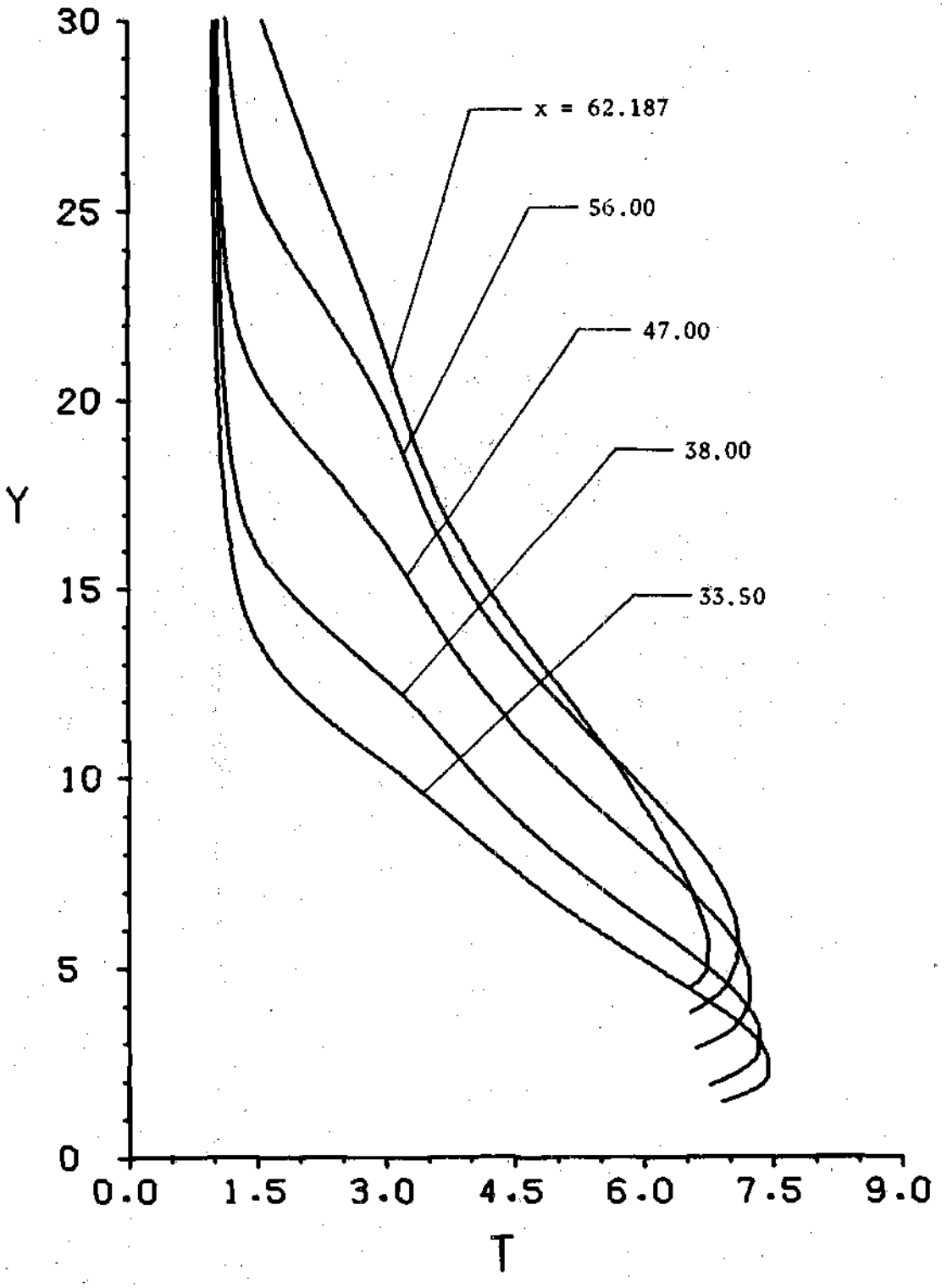

Figure 16. Temperature, $33.50 \leq x < 64.437$

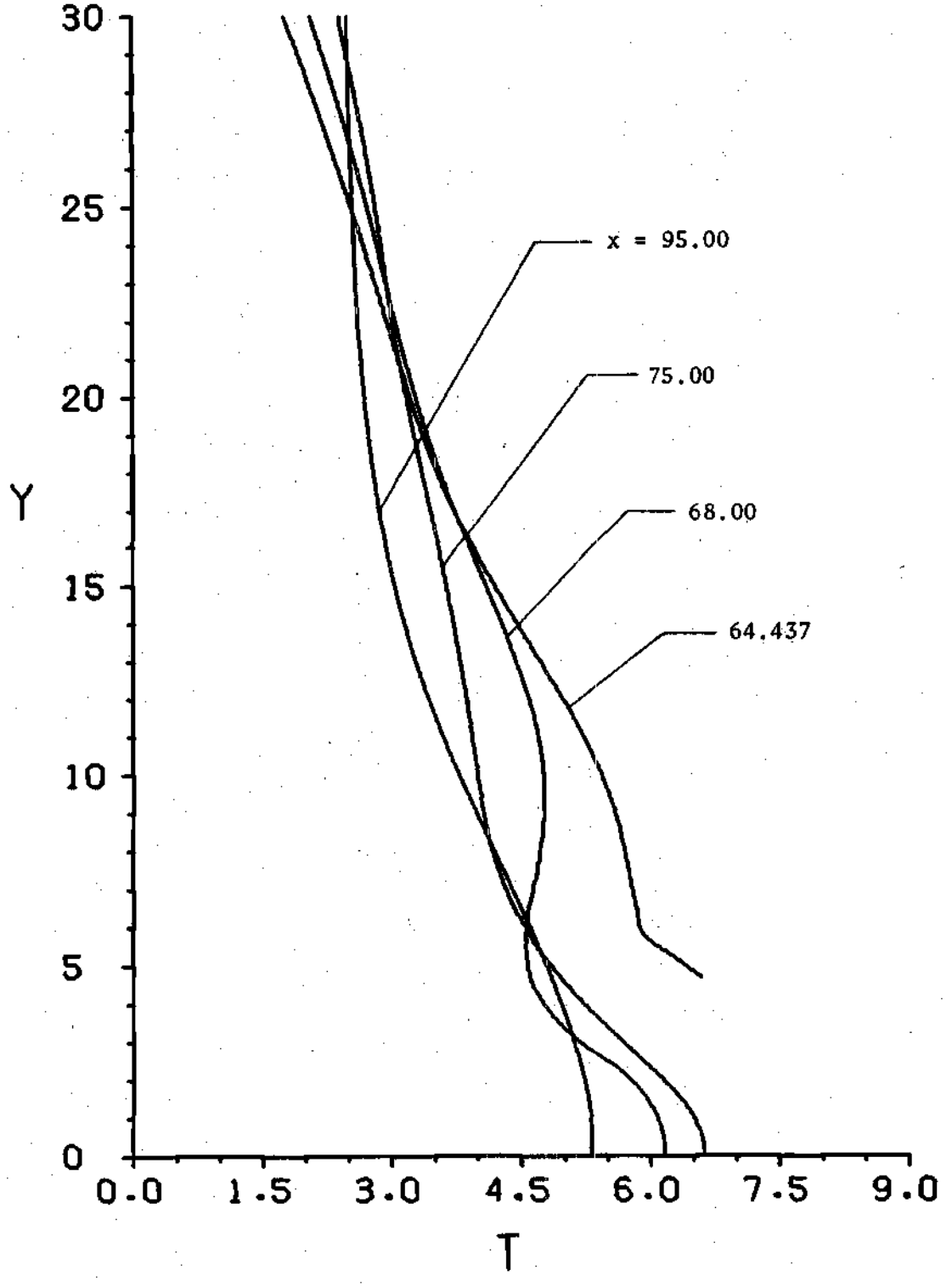

Figure 17. Temperature, $x \geq 64.437$

the nonequilibrium distribution functions are dispersed over a larger range of velocities than may have been initially expected. The functions are obviously smeared due to the interactions of the free-stream molecules with a small number of the molecules emitted from the wall. At the leading edge the temperature rises sharply. Although a stagnation point does not exist, the flow slows down considerably and converts much of its directed energy into thermal energy.

As the flow begins to adjust to the presence of the body and its corresponding temperature, the temperature of the gas adjacent to the surface decreases. The rise in temperature in the viscous surface layer can be seen in all of the plotted profiles from $x = 22.25$ to $x = 62.187$. An inflection occurs near the free-stream limits of the temperature profiles from $x = 33.50$ to $x = 62.187$. This behavior is similar to that found in the x-component of velocity and originates from the same cause, namely, making observations through the shock in the y-direction rather than normal to it.

At $x = 64.437$ a different trend in the profile can be seen. The surface temperature has increased over that at the previous stations and in moving away from the surface the temperature decreases rapidly for a short length and then assumes a normal character. This is a consequence of phenomena taking place in the wake region of the body. In the wake at $x = 68.00$ an inflection in the temperature occurs near $y = 5.75$. This inflection is associated with the maximum height of the training edge of 4.75 at $x = 65.00$. Below $y = 5.75$ the temperature is established primarily by the conduction of heat from the rear surface and by the decrease in total velocity as the center line is

approached. Above this point it is primarily determined by the flow over the slant surface. In the next profile, the wake region sustains its temperature not only by conduction and velocity deceleration, but also by diffusion of molecular kinetic energy from the flow past the slant surface. Eventually, as for the other properties, the temperature begins to return toward the free-stream value as indicated at x = 95.00. The rate of change is generally slower than for any of the other properties.

Surface Variations

The variation of number density, tangential velocity, temperature, and wall density coefficients along the slant surface of the wedge are plotted in Figures 18 through 21. For the reason previously mentioned, the trailing edge point has been omitted. It should also be noted that the abscissa does not represent the distance measured along the surface, but indicates the location of the surface point measured from x = 0.0 parallel to the center line. The latter may be obtained by using the transformation

$$d = (x - 20.00)\ \sec(6.026^\circ) \qquad 20 \leq x \leq 65$$

where d is the distance from the leading edge measured along the surface and x is the location of the point relative to the previously described coordinate system.

Number Density at the Surface

The variation of the wall number density is given in Figure 18. The curve starts well above its free molecular limit of 1.29 and

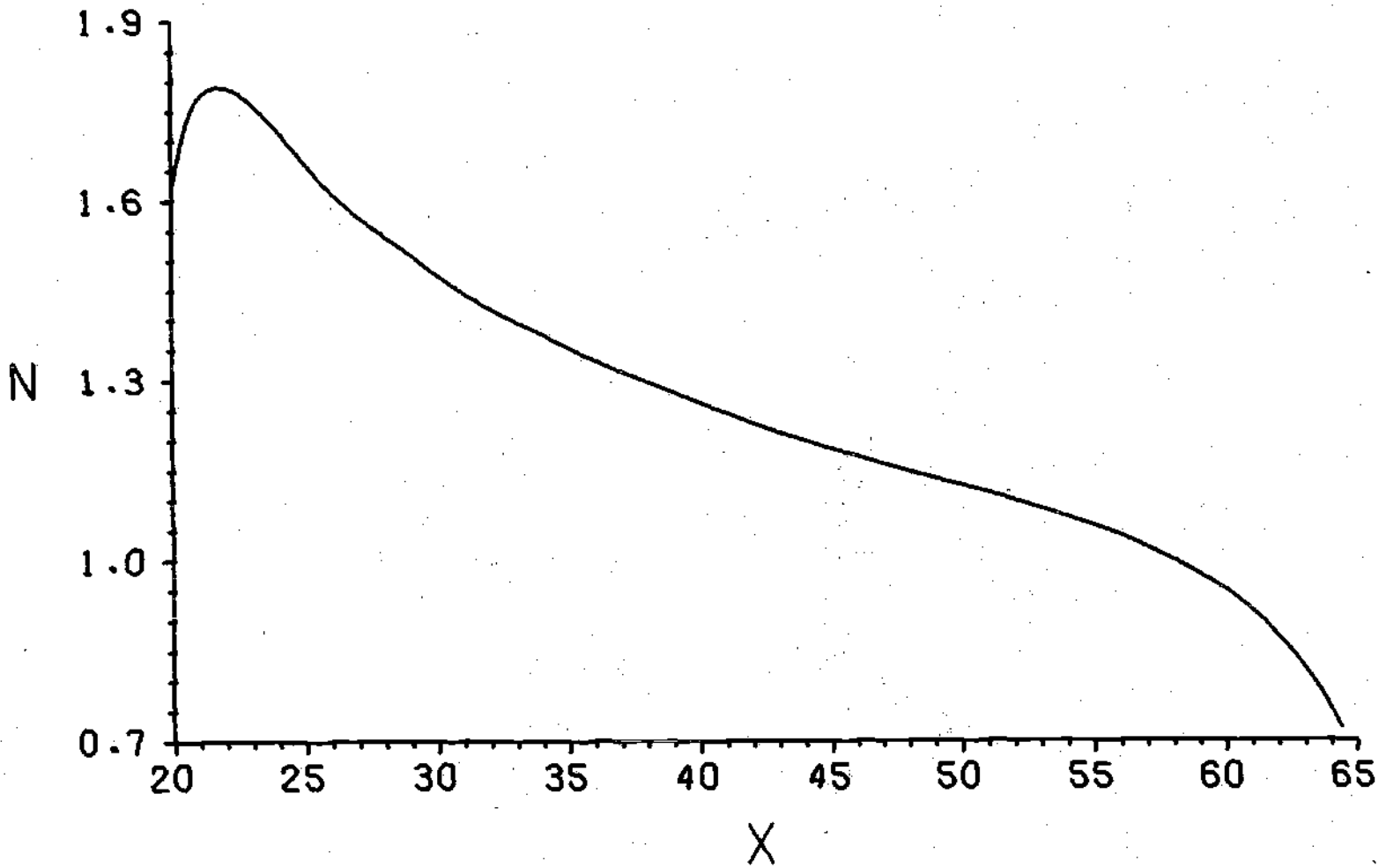

Figure 18. Variation of the Number Density at the Surface

increases rapidly, reaching a peak near x = 22.00. Proceeding downstream, the number density decrease. Around x = 55.00 the number density drops off rapidly due to the upstream influence that the wake has near the trailing edge of the body. The density in the near wake is quite low and consequently the flow begins to adjust to this.

Tangential Velocity at the Surface

The surface tangential velocity (UT), or slip velocity as it is frequently called, is seen to decrease rapidly from its peak value at the leading edge (Figure 19). The decrease becomes more moderate near x = 25.00 and tapers off very slowly beginning at x = 40.00. Close to x = 55.00 the decrease has stopped and an increase follows. This velocity nowhere reaches the continuum no-slip condition. The effects of the wake are again easily observed near the trailing edge where the flow accelerates in anticipation of the upcoming expansion.

Gas Temperature at the Surface

Figure 20 indicates that the surface gas temperature has a behavior very similar to the slip velocity. At x = 20.00, the temperature shows a marked decrease which slows down as the trailing edge is approached. Whereas a reversal in slope takes place near x = 56.00 in the case of other properties, here it occurs at x = 61.00. The reason for the increase near the trailing edge is not yet understood, but has also been observed in the computation of flows over flat plates.[30]

Wall Number Density Coefficients

The variation of wall number density coefficients used in the diffuse reflection model is presented in Figure 21. Under the assumptions given in Appendix D, this plot also can be made to represent the

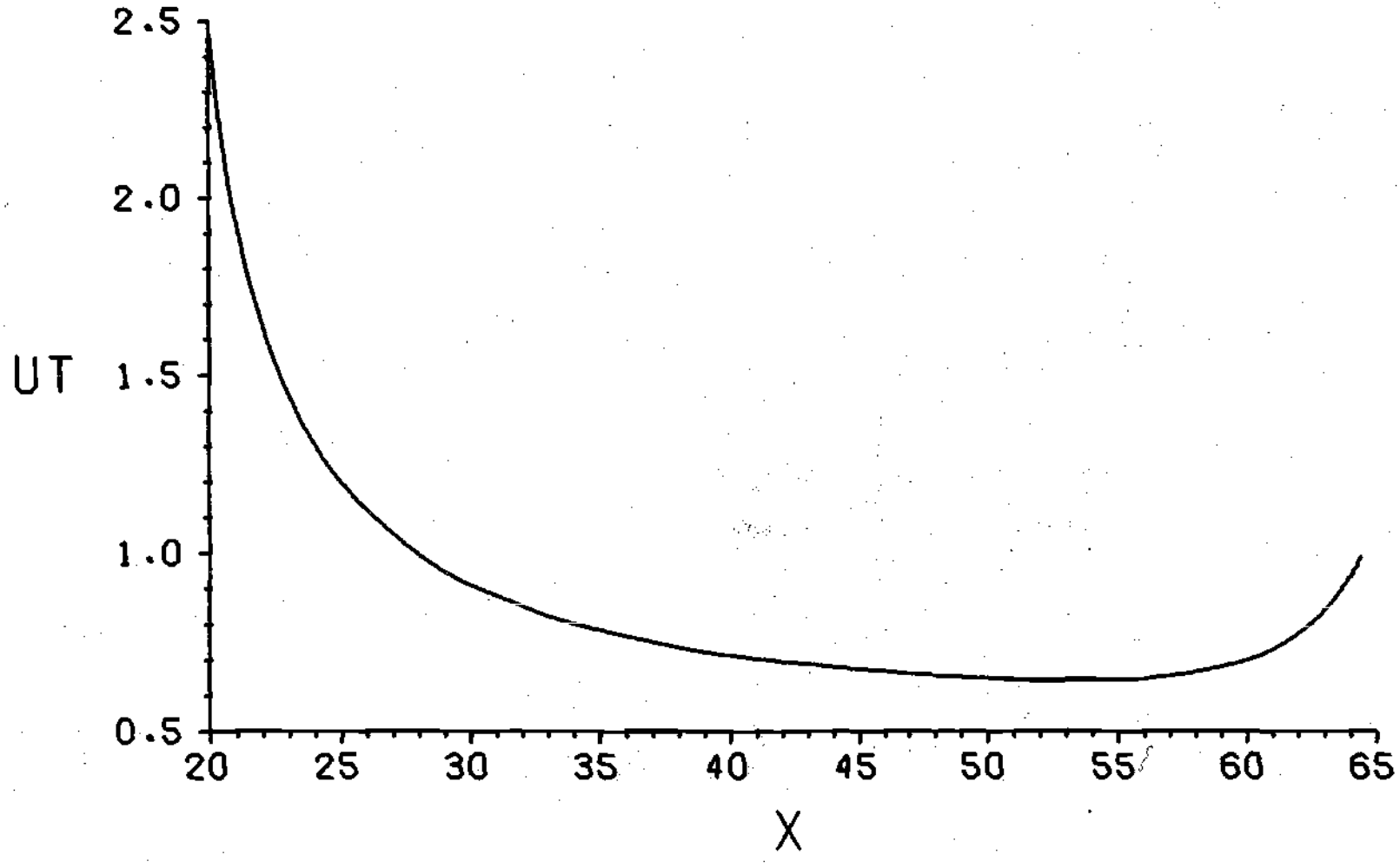

Figure 19. Variation of the Tangential Velocity at the Surface

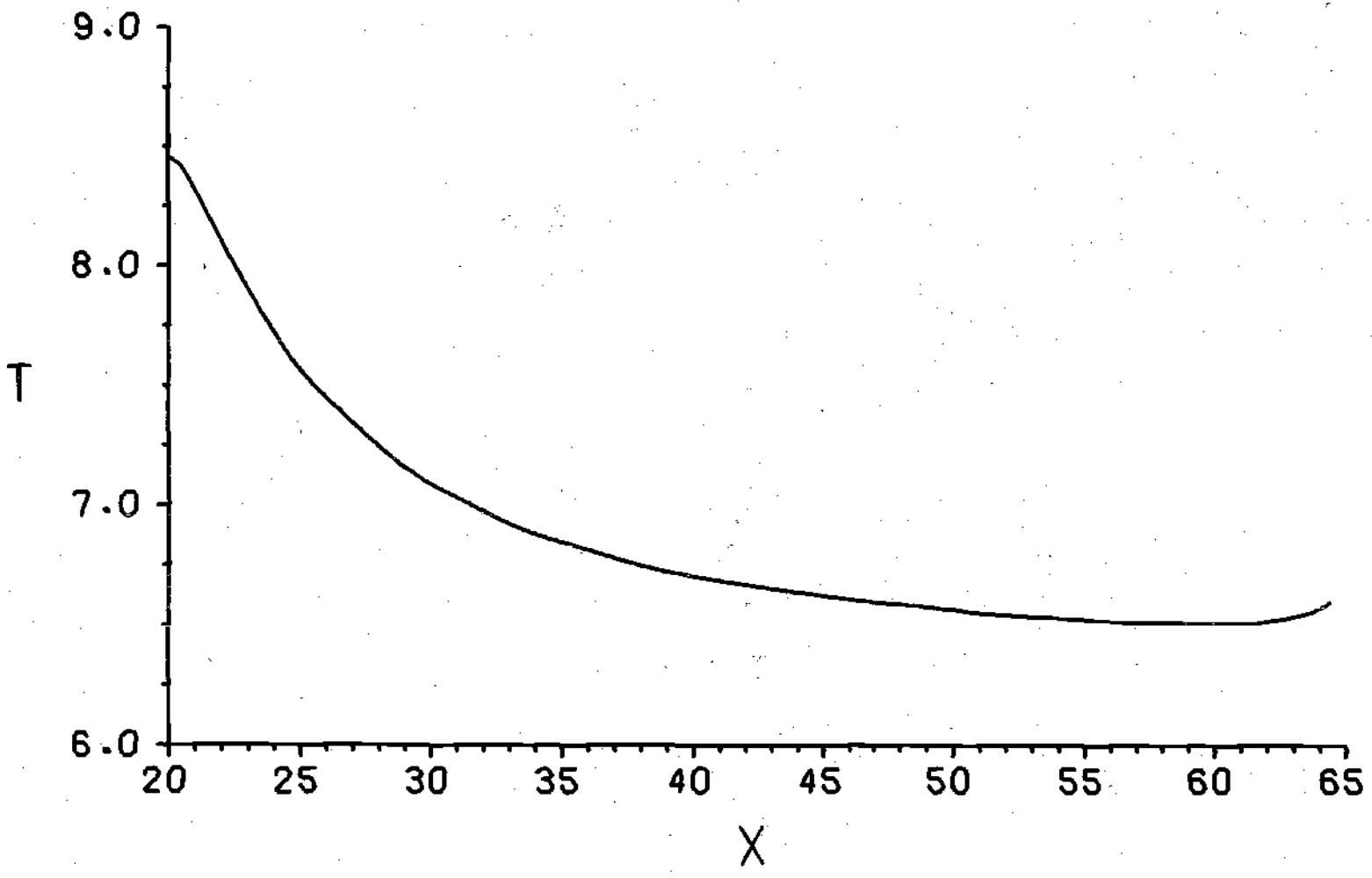

Figure 20. Variation of the Gas Temperature at the Surface

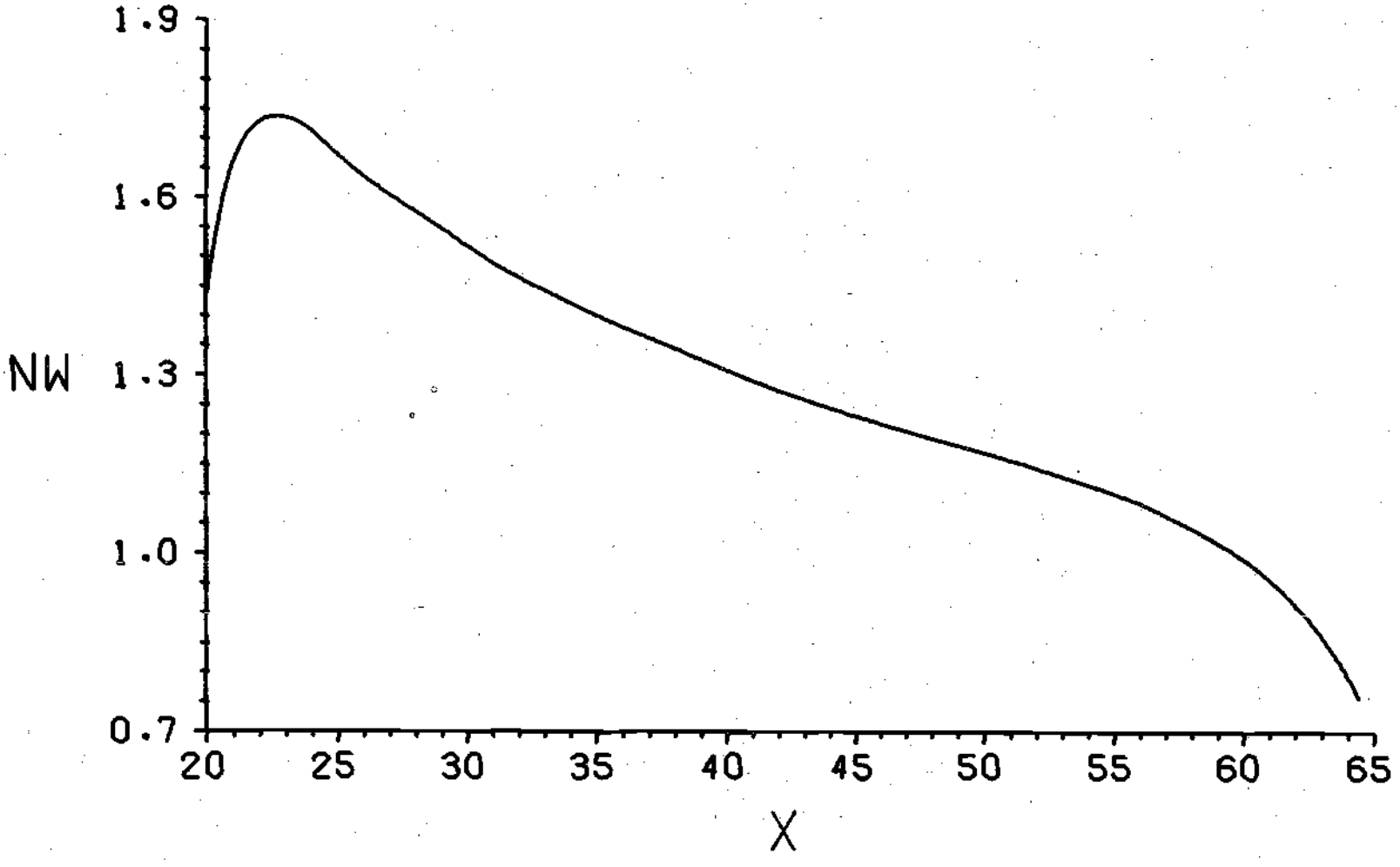

Figure 21. Variation of the Wall Number Density Coefficients Along the Surface

nondimensional pressure in a small cavity with the same temperature as the body and opened to the flow by a small orifice normal to the surface. The magnitude and slope of the curve follows very closely the surface number density variation. The peak in the coefficient plot is slightly reduced and shifted downstream by approximately a free-stream mean free path. The remainder of the curve is generally greater than the surface density plot by about 0.04 units. As in the other surface plots, a change in trend occurs near the trailing edge.

Comparison with Experiment

As discussed in the introduction, the availability of experimental data in the literature for hypersonic, low density flow past a wedge is limited. Most of the results have been obtained for flows at Mach numbers near 20 and in diatomic gases. The data which is available for flow situations similar to those of this problem, contain only wall pressure or surface number flux measurements. These can be compared with the wall number density coefficients under the assumptions of Appendix D whereby a wall pressure may be inferred.

In the two comparisons which follow, the abscissa (D) represents the nondimensional distance, $\hat{d}/\lambda_\infty$, along the surface of the wedge from the leading edge. In Figure 22, the inferred pressures are compared with the results of Reference 15. The data were obtained from a symmetric wedge of 5° half-angle. The Mach number was 8.1 in air and the wall-to-stagnation temperature ratio was 0.56. The plots generally show the same trends. The pressures obtained in the solution have an overall higher value than those of the experiment, except near the trailing edge. In the experiment the wedge was sufficiently long that

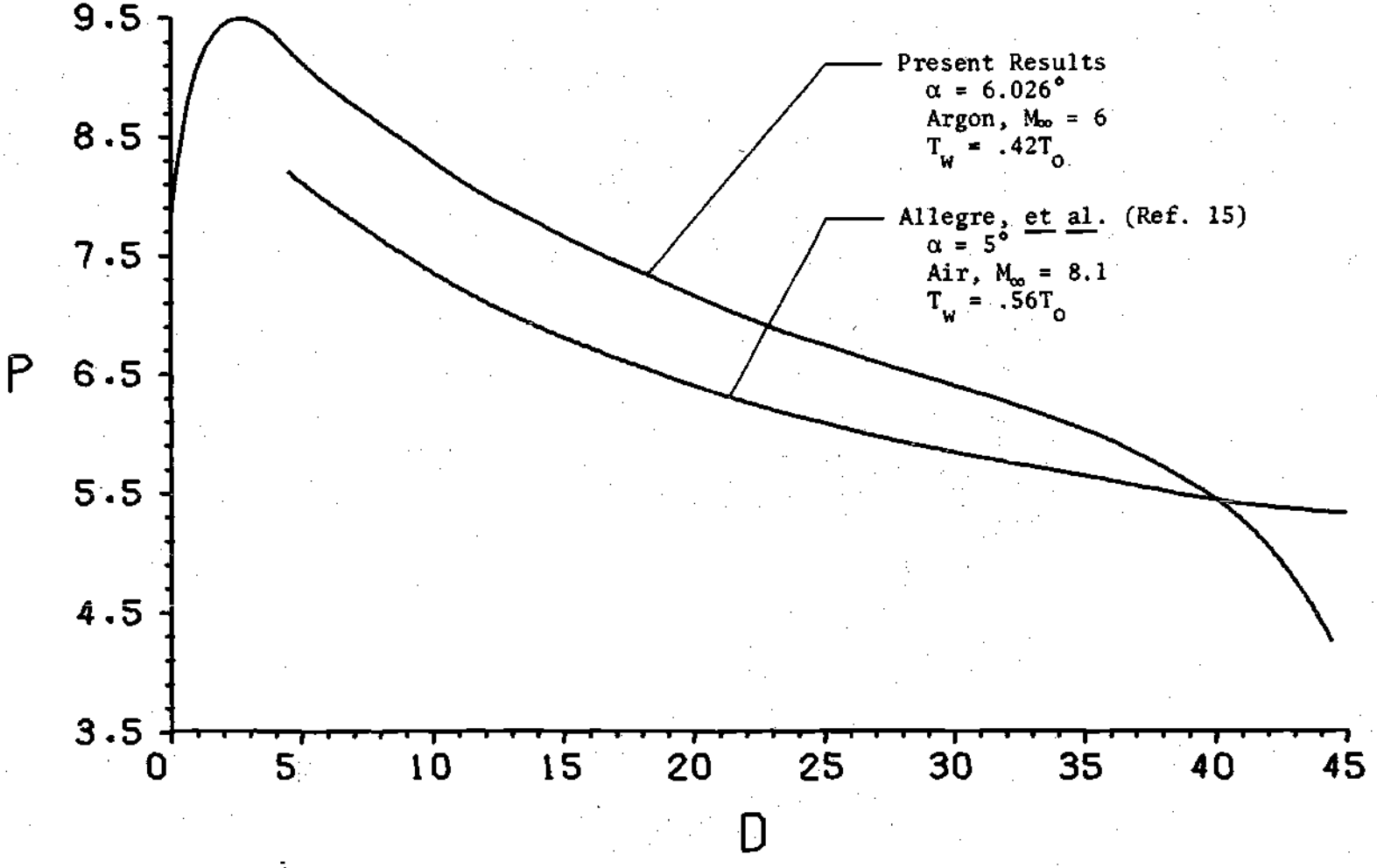

Figure 22. Wall Pressure

the trailing edge effects are not detected in the scale of the graph shown.

Horstman[31] has obtained the number flux on the surface of a 10° half-angle wedge for Mach numbers between 22 and 28 in helium and for the range from 11 to 13 in air for varying wall temperatures. In that report the number flux, $\hat{N}_f$, was evaluated as follows:

$$\hat{N}_f = \frac{\hat{p}}{m\sqrt{2\pi\hat{T}_w}}$$

The pressure $\hat{p}$ was measured in a cavity opened to the surface from which the number flux was obtained. Upon nondimensionalizing $\hat{N}_f$ by the free molecular number flux, Horstman found the results to be independent of the Mach number, the gas, and the wall temperature.

For the present theoretical studies the number flux may be obtained from the solution by using the inferred pressures (see Appendix D). A simple relation results between the number flux and the wall number density coefficients given by

$$N_f = \frac{\hat{n}_w}{\hat{n}_{w,FM}}$$

where $N_f = \hat{N}_f/\hat{N}_{f,FM}$ is the nondimensional form of number flux and $\hat{n}_{w,FM}$ is the free molecular wall number density coefficient. For the computer solution $\hat{n}_{w,FM} = .998\ \hat{n}_\infty$; therefore,

$$N_f \doteq n_w$$

Figure 23 shows a comparison of the experimental data with the

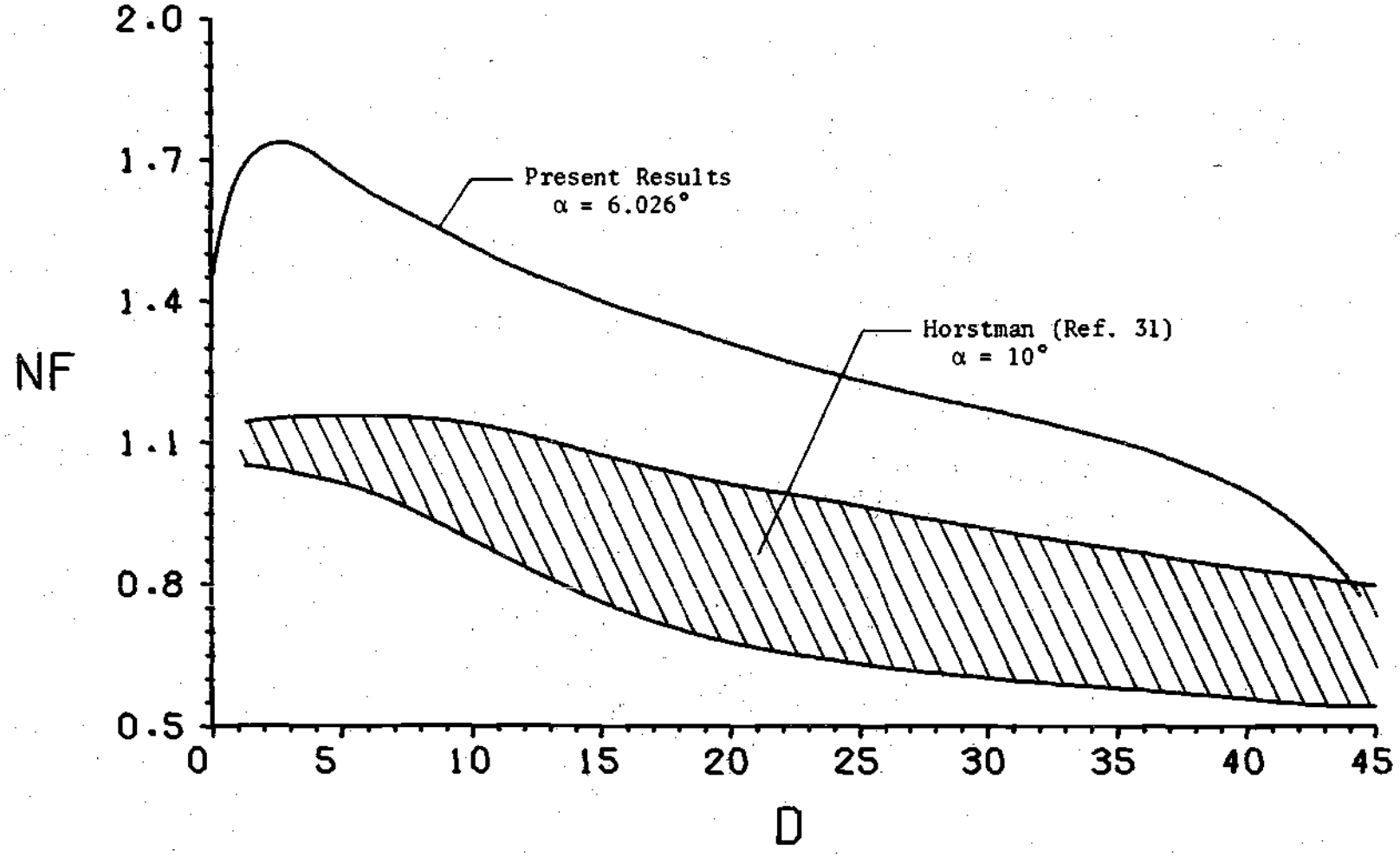

Figure 23. Number Flux

results of the present solution. Due to the scatter in the data, the experimental measurements appear in the shaded region. The computed number flux values, which have been nondimensionalized by the free molecular value are higher because of the lesser wedge half-angle of the present solution. However, the overall trends are similar. Near the leading edge there is some indication of a peak or plateau resembling the results obtained analytically. As in the previous comparison, trailing edge effects in the experiment are not noticeable due to the length of the experimental wedge.

At present, no data are available which can be compared with other macroscopic properties and remaining surface variations obtained in this dissertation. Clearly, more experimental data are required before any quantitative comparisons can be performed.

CHAPTER V

CONCLUSIONS

The rarefied flow field about a symmetric wedge of finite length immersed in a hypersonic stream of a monatomic gas has been computed. The Boltzmann equation was solved with the collision integral replaced by the BGK relaxation model. The numerical technique for obtaining the solution was the discrete ordinate method with integration performed along molecular path lines.

Emphasis was placed on determining the properties in the region near the surface of the forebody and the grid points were chosen with this impetus in mind. The first order numerical scheme employed, although relatively slow in converging, was quite stable even for the extremely crude estimate of a completely uniform flow as an initial guess.

Several interesting phenomena are observed in the numerical results for the macroscopic properties. The "upstream influence" effect is particularly noticeable in the vicinities of the leading and trailing edges. Ahead of the leading edge all of the physical properties deviated from their free-stream values, with the temperature being the most sensitive indicator of this disturbance. Since no other results are available for similar flow conditions, a direct comparison cannot be made; however, a corresponding behavior has been observed experimentally in the number density profiles ahead of the leading edge of flat plates at high Mach numbers in nitrogen.

The effects of the "upstream influence" near the trailing edge

can be seen in all the property profiles beginning at about x = 56.00. The nature of the developed profiles begins to change slightly at first and then more rapidly as the trailing edge is approached. The surface variation plots indicate that pressure and density decrease rapidly in this region whereas the gas temperature and tangential velocity increase.

These phenomena would have gone undetected if an initial value method had been used. The closed boundary approach indicates the extensiveness of the effects that the upstream random motion of the molecules have in the formation of a rarefied flow field.

Due to a lack of available data in the literature, a realistic comparison could only be made of the forebody wall surface pressures. The theoretical results obtained compared favorably with those from experiments. The solution predicts a peak surface pressure at about three mean free paths downstream of the leading edge followed by a continued decrease.

The surface tangential velocity and surface temperature plots indicate that near the leading edge there is a rapid adjustment toward the no-slip condition at the wall. Yet the rate of accommodation quickly declines after several mean free paths with the result that there is both a velocity slip and temperature jump over the entire slant surface. The solution also presents the initial formation and development of the shock wave structure which eventually assumes the same thickness as the wedge itself. Compressions and expansions can be identified in the profiles. The body length of 45 mean free paths was, as expected, insufficient to allow the formation of the classical continuum,

viscous interaction image of the flow with a distinct shock and boundary layer.

Although computational emphasis was not placed on detailed wake calculations, the results demonstrate the capability of the technique in addressing the solution of this problem. General wake characteristics are present in the results, such as appropriate streamline directions, number densities, and temperature variations.

The principal drawback of this method of solution is the considerable computer time required in obtaining the results. This is a consequence of having to solve the equation not only in the physical space variables but also in velocity space. The solution time is further increased as a result of the first order numerical methods employed which reduces the speed of convergence. Since nothing can be done to lessen the number of independent variables, a continued effort in augmenting the exactness of the numerical techniques may assist in increasing the rate of convergence and hence the overall time.

The results of this dissertation indicate that the kinetic theory approach using the Boltzmann equation with relaxation models can be employed to arrive at meaningful results for flow situations of simple geometries. The results obtained appear realistic, but quantitative verification must await the advent of new experimental data. In applying this approach to other two-dimensional flows, one must be acutely aware of the problems of computer time; and in altering this technique, numerical efforts must be concentrated on the specific regions of interest. Currently, using the basic methods of this thesis one might approach the problems of unsymmetric wedges, wedges at angles of attack,

a variety of wedge-plate combinations, plumes, and blunt body situations in both monatomic and diatomic gas flows with a reasonable assurance of obtaining satisfactory results.

APPENDIX A

DISCRETE ORDINATE METHOD

The discrete ordinate method is a numerical technique useful in the solution of differential, integral, and integro-differential equations of more than one independent variable. The technique is such that one or more, but not all, of the independent variables are discretized; that is, specific values are taken for these independent variables. The equation or equations are still continuous in one or more of the remaining independent variables; and, as such, other techniques, whether numerical or mathematical, may be applied to them. The problem has been transformed into a set of continuous equations or approximations, one for each discrete ordinate or combination thereof. The best choice of the points for the discrete ordinates depends on the nature of the problem.

In this research the problem is to solve a system of integro-differential equations in four independent variables. The forms of the equations to be solved are

$$v_x \frac{dg}{dx} = \nu(G - g)$$

$$\left(\frac{dy}{dx}\right)_{char} = \frac{v_y}{v_x}$$

where

$$G = G(x,y,v_x,v_y;n,u_x,u_y,T)$$

$$\nu = \nu(x,y;n,T)$$

and n, u_x, u_y, T are related to specific moments of g. For this particular problem it is appropriate to discretize the independent variables v_x, v_y. Since all macroscopic properties are the results of moments of the dependent variables, the discrete ordinates have been chosen to easily approximate these integrals. Thus, the discrete ordinate points are picked such that they are the quadrature points in the approximating quadrature scheme.

An example will best demonstrate this point. The number density is given by

$$n = \int_{-\infty}^{\infty} \int_{-\infty}^{\infty} g \, dv_x dv_y$$

To perform this integral numerically, n is approximated by

$$n = \sum_{k=1}^{k_e} \sum_{\ell=1}^{\ell_e} w_k w_\ell g(v_k, v_\ell)$$

where (w_k, v_k) and (w_ℓ, v_ℓ) are the weight-quadrature point pairs and depend on the choice of quadrature used. The v_k's and v_ℓ's given here are used as the discrete ordinates. The accuracy of the choice of points may be ascertained by the accuracy with which the resultant summation is able to approximate the integration for functional forms similar to those expected in the solution. Further information can be found in References 19 and 32.

APPENDIX B

DERIVATION OF CHARACTERISTICS

The equations to be solved by the characteristic method are of the form,

$$v_k \frac{\partial f}{\partial x} + v_\ell \frac{\partial f}{\partial y} = I \tag{B-1}$$

where v_k and v_ℓ are the discrete velocities, f is representative of either g or h, and I denotes the appropriate collision term.

To determine the characteristic lines for this equation, two arbitrary coordinates β and γ are chosen

$$\beta = \beta(x,y)$$

$$\gamma = \gamma(x,y)$$

and

$$f = f(\beta,\gamma)$$

Equation (B-1) can be written as

$$\frac{\partial f}{\partial \beta}\left(v_k \frac{\partial \beta}{\partial x} + v_\ell \frac{\partial \beta}{\partial y}\right) + \frac{\partial f}{\partial \gamma}\left(v_k \frac{\partial \gamma}{\partial x} + v_\ell \frac{\partial \gamma}{\partial y}\right) = I \tag{B-2}$$

Now assuming that $\beta(x,y)$ is chosen such that

$$v_k \frac{\partial \beta}{\partial x} + v_\ell \frac{\partial \beta}{\partial y} = 0 \tag{B-3}$$

Equation (B-2) reduces to

$$\frac{\partial f}{\partial \gamma}\left(v_k \frac{\partial \gamma}{\partial x} + v_\ell \frac{\partial \gamma}{\partial y}\right) = \mathbb{I} \tag{B-4}$$

Equation (B-3) may also be written in the form

$$\frac{\partial \beta}{\partial x} \Big/ \frac{\partial \beta}{\partial y} = - \frac{v_\ell}{v_k} \tag{B-5}$$

The following relations also hold

$$d\beta = \frac{\partial \beta}{\partial x} dx + \frac{\partial \beta}{\partial y} dy \tag{B-6}$$

$$d\gamma = \frac{\partial \gamma}{\partial x} dx + \frac{\partial \gamma}{\partial y} dy \tag{B-7}$$

Moving along a line of constant β or $d\beta = 0$, (B-6) becomes

$$\frac{\partial \beta}{\partial x} dx + \frac{\partial \beta}{\partial y} dy = 0 \tag{B-8}$$

Upon rearranging terms this gives

$$\frac{\partial \beta}{\partial x} \Big/ \frac{\partial \beta}{\partial y} = - \frac{dy}{dx} \tag{B-9}$$

The left-hand side of (B-9) is the same as that of (B-5); therefore

$$\left(\frac{dy}{dx}\right)_{\beta=\text{const.}} = \frac{v_\ell}{v_k} \tag{B-10}$$

This is the slope of the line when $\beta(x,y)$ is a constant. It will be subsequently shown that this line is a characteristic line, for it reduces Equation (B-1) to a total differential equation.

Now

$$df = \frac{\partial f}{\partial \beta} d\beta + \frac{\partial f}{\partial \gamma} d\gamma \tag{B-11}$$

Along a line of constant β

$$df = \frac{\partial f}{\partial \gamma} d\gamma \tag{B-12}$$

Upon replacing $d\gamma$ as given by Equation (B-7) one obtains

$$df = \frac{\partial f}{\partial \gamma} \left(\frac{\partial \gamma}{\partial x} dx + \frac{\partial \gamma}{\partial y} dy \right) \tag{B-13}$$

After algebraic manipulations this results in

$$df = \frac{\partial f}{\partial \gamma} \left[\frac{\partial \gamma}{\partial x} + \frac{\partial \gamma}{\partial y} \left(\frac{dy}{dx} \right)_{\beta=\text{const.}} \right] dx \tag{B-14}$$

Using Equation (B-10), (B-14) becomes

$$df = \frac{\partial f}{\partial \gamma} \left(v_k \frac{\partial \gamma}{\partial x} + v_\ell \frac{\partial \gamma}{\partial y} \right) \frac{dx}{v_k} \tag{B-15}$$

or

$$v_k \left(\frac{df}{dx} \right)_{\beta=\text{const.}} = \frac{\partial f}{\partial \gamma} \left(v_k \frac{\partial \gamma}{\partial x} + v_\ell \frac{\partial \gamma}{\partial y} \right) \tag{B-16}$$

A comparison of Equations (B-4) and (B-16) results in

$$v_k \left(\frac{df}{dx} \right)_{\beta=\text{const.}} = I$$

subject to the constraint

$$\left(\frac{dy}{dx}\right)_{\beta=\text{const.}} = \frac{v_\ell}{v_k}$$

APPENDIX C

SOLUTION GRID NETWORK

The grid lines used in this dissertation are given in Tables 1 and 2 of this appendix. These lines were chosen in order to provide decreasing interval sizes as the wedge surfaces are approached and to position a large number of grid points in the vicinities of the leading and trailing edges, where changes in the gradients are expected to be large.

The grid points at which solutions were obtained are the points of intersection of the grid lines with each other or with the surfaces of the wedge. The coordinates of these surface points are given in Table 3. Those points contained within the wedge are not considered, as they serve no purpose in the solution.

Table 1. The X-Grid Lines

0.000	5.000	10.000	13.000
16.000	17.000	18.000	19.000
19.500	20.000	20.562	21.125
21.687	22.250	22.812	23.375
23.937	24.500	26.000	27.500
29.000	31.250	33.500	35.750
38.000	42.500	47.000	49.250
51.500	53.750	56.000	57.500
59.000	60.500	61.062	61.625
62.187	62.750	63.312	63.875
64.437	65.000	65.500	66.000
67.000	68.000	69.000	72.000
75.000	80.000	85.000	95.000
105.000	125.000	145.000	165.000
185.000			

Table 2. The Y-Grid Lines

0.000	0.475	0.950	1.425
1.900	2.375	2.850	3.325
3.800	4.275	4.750	5.250
5.750	6.250	7.000	8.000
9.000	10.000	12.000	14.000
16.000	18.000	20.000	22.000
25.000	30.000	35.000	40.000
50.000	60.000	70.000	

Table 3. The Coordinates of the Surface Grid Points

x	y	x	y
20.000	0.0000	57.500	3.9583
20.562	0.0594	59.000	4.1167
21.125	0.1188	60.500	4.2750
21.687	0.1781	61.062	4.3344
22.250	0.2375	61.625	4.3937
22.812	0.2969	62.187	4.4531
23.375	0.3563	62.750	4.5125
23.937	0.4156	63.312	4.5719
24.500	0.4750	63.875	4.6312
26.000	0.6333	64.437	4.6906
27.500	0.7917	65.000	4.7500
29.000	0.9500	65.000	4.2750
31.250	1.1875	65.000	3.8000
33.500	1.4250	65.000	3.3250
35.750	1.6625	65.000	2.8500
38.000	1.9000	65.000	2.3750
42.500	2.3750	65.000	1.9000
47.000	2.8500	65.000	1.4250
49.250	3.0875	65.000	0.9500
51.500	3.3250	65.000	0.4750
53.750	3.5625	65.000	0.0000
56.000	3.8000		

APPENDIX D

INFERENCE OF WALL PRESSURE FROM THE WALL NUMBER DENSITY COEFFICIENT

The wall number density coefficient arises in determining the zero net mass flux condition at the surface. This coefficient represents the number density of the diffuse distribution function on the surface. When a pressure tap of dimensions smaller than the local mean free path is placed normal to a surface, initially there is a large flux of molecules into this orifice. Within a short time interval a steady state condition will be reached in which the net flux entering the tap will be balanced by the flux leaving. The effluxing molecules should, as a result of numerous collisions, have an equilibrium velocity distribution with the same temperature as that of the orifice. If the temperature in the cavity is the same as the wall temperature, then the distribution will be identical in form to the diffuse reflection function except for the number density term. Assuming that the distribution function for molecules which influx is independent of that for those in efflux (i.e., free molecular flow), then, once equilibrium is reached, the condition of no mass build up requires that the number density be identical to $\hat{n}_w$.

Since the gas in the cavity should behave as an ideal gas, then $\hat{p}$, the pressure, is given by

$$\hat{p} = \hat{n}_w k \hat{T}_w$$

The nondimensional pressure $\hat{p}/\hat{p}_\infty$ is then

$$p = n_w T_w$$

BIBLIOGRAPHY

1. R. J. Vidal and C. E. Wittliff, "Hypersonic Low Density Studies of Blunt and Slender Bodies," Rarefied Gas Dynamics, Third Symposium, Edited by J. A. Laurmann, Academic Press, Vol. II, p. 343 (1963).

2. R. J. Vidal and J. A. Bartz, "Surface Measurements on Sharp Flat Plates and Wedges in Low-Density Hypersonic Flow," AIAA Journal, 7, p. 1099 (1969).

3. M. Becker, "Flat Plate Flow Field and Surface Measurements from Merged Layer Into Transition Regime," Rarefied Gas Dynamics, Sixth Symposium, Edited by L. Trilling and H. Y. Wachman, Academic Press, Vol. I, p. 515 (1969).

4. R. L. Chuan and S. A. Waiter, "Experimental Study of Hypersonic Flow near the Leading Edge of a Thin Flat Plate," Rarefied Gas Dynamics, Third Symposium, Edited by J. A. Laurmann, Academic Press, Vol. II, p. 328 (1963).

5. E. S. Moulic and G. J. Maslach, "Induced Pressure Measurements on a Sharp-Edged Insulated Flat Plate in Low Density Hypersonic Flow," Rarefied Gas Dynamics, Fifth Symposium, Edited by C. L. Brundin, Academic Press, Vol. II, p. 971 (1967).

6. I. E. Vas and J. Allegre, "The N-4 Hypersonic Low Density Facility and Some Preliminary Results on a Sharp Flat Plate," Rarefied Gas Dynamics, Fifth Symposium, Edited by C. L. Brundin, Academic Press, Vol. II, p. 1015 (1967).

7. W. J. McCroskey, S. M. Bogdonoff, and A. P. Genchi, "Leading Edge Flow Studies of Sharp Bodies in Rarefied Hypersonic Flow," Rarefied Gas Dynamics, Fifth Symposium, Edited by C. L. Brundin, Academic Press, Vol. II, p. 1047 (1967).

8. P. J. Harbour and J. H. Lewis, "Preliminary Measurements of the Hypersonic Rarefied Flow Field on a Sharp Flat Plate Using an Electron Beam Probe," Rarefied Gas Dynamics, Fifth Symposium, Edited by C. L. Brundin, Vol. II, p. 1031 (1967).

9. R. S. Hickman, "Hypersonic Transitional Flow at the Leading Edge of a Sharp Flat Plate," Rarefied Gas Dynamics, Sixth Symposium, Edited by L. Trilling and H. Y. Wachman, Academic Press, Vol. I, p. 583 (1969).

10. F. W. Vogenitz, J. E. Broadwell, and G. A. Bird, "Leading Edge Flow by the Monte Carlo Direct Simulation Technique," AIAA Journal, 8, p. 504 (1968).

11. S. Rudman and S. G. Rubin, "Hypersonic Viscous Flow Over Slender Bodies with Sharp Leading Edges," AIAA Journal, 6, p. 1883 (1968).

12. H. K. Cheng, J. G. Hall, T. C. Golian, and A. Hertzberg, "Boundary-Layer Displacement and Leading-Edge Bluntness Effects in High-Temperature Hypersonic Flow," Journal of the Aerospace Sciences, 28, p. 353 (1961).

13. A. B. Huang, "Kinetic Theory of the Rarefied Supersonic Flow over a Finite Plate," Rarefied Gas Dynamics, Sixth Symposium, Edited by L. Trilling and H. Y. Wachman, Academic Press, Vol. I, p. 529 (1969).

14. D. P. Giddens and A. B. Huang, "Hypersonic Flow over a Finite Flat Plate According to the Bhatnagar-Gross-Krook Model," Presented at the Eighth International Symposium on Rarefied Gas Dynamics (to be published) (1972).

15. J. Allegre, G. Herpe, and D. Faulmann, "Measurements of Pressure Distribution, Drag and Lift on Flat Plates and Wedges at Mach 8 in Rarefied Gas Flow," Rarefied Gas Dynamics, Sixth Symposium, Edited by L. Trilling and H. Y. Wachman, Academic Press, Vol. I, p. 465 (1969).

16. C. C. Horstman, "Surface Pressures and Shock-Wave Shapes on Plates and Wedges in Low-Density Hypersonic Flow," Rarefied Gas Dynamics, Sixth Symposium, Edited by L. Trilling and H. Y. Wachman, Academic Press, Vol. I, p. 593 (1969).

17. F. W. Vogenitz, G. A. Bird, J. E. Broadwell, and H. Rungaldier, "Theoretical and Experimental Study of Rarefied Supersonic Flow about Several Simple Shapes," AIAA Journal, 6, p. 2388 (1968).

18. W. L. Chow and R. E. Eilers, "Hypersonic Low-Density Flow past Slender Wedges," AIAA Journal, 6, p. 177 (1968).

19. D. P. Giddens,"Study of Rarefied Gas Flow by the Discrete Ordinate Method,"Georgia Institute of Technology, Ph.D. Thesis (1966).

20. A. B. Huang and D. L. Hartley, "Kinetic Theory of the Sharp Leading Edge Problem in Supersonic Flow," Physics of Fluids, 12, p. 96 (1969).

21. A. B. Huang and P. F. Hwang, "Kinetic Theory of the Sharp Leading Edge Problem II. Hypersonic Flow," International Astronautical Federation Paper RE 63 (1968).

22. A. B. Huang and P. F. Hwang, "Supersonic Leading Edge Problem according to the Ellipsoidal Model," Physics of Fluids, 13, p. 309 (1970).

23. P. F. Hwang, "A Kinetic Theory Description of Rarefied Gas Flows with the Effect of Rotational Relaxation," Georgia Institute of Technology, Ph.D. Thesis (1971).

24. A. B. Huang, P. F. Hwang, D. P. Giddens, and R. Srinivasan, "High-Speed Leading Edge Problem," Physics of Fluids, 16, p. 814 (1973).

25. P. L. Bhatnagar, E. P. Gross, and M. Krook, "A Model for Collision Processes in Gases," Physical Review, 94, p. 511 (1954).

26. B. Carnahan, H. A. Luther, and J. O. Wilkes, Applied Numerical Methods, John Wiley & Sons, Inc., p. 90 (1969).

27. F. B. Hildebrand, Advanced Calculus for Engineers, Prentice-Hall, Inc., p. 107 (1955).

28. Z. Kopal, Numerical Analysis, Chapman & Hall Ltd., p. 145 (1961).

29. S. Chapman and T. G. Cowling, The Mathematical Theory of Non-Uniform Gases, Cambridge University Press, p. 223 (1961).

30. D. P. Giddens and R. Srinivasan, personal communications, School of Aerospace Engineering, Georgia Institute of Technology, Atlanta, Georgia.

31. C. C. Horstman, "Number Flux Measurements on Sharp Plates and Wedges in the Kinetic Flow Regime," personal communications, Ames Research Center, NASA.

32. A. B. Huang, "A General Discrete Ordinate Method for the Dynamics of Rarefied Gases," School of Aerospace Engineering, Georgia Institute of Technology, Rarefied Gas Dynamic and Plasma Lab., Report No. 4 (1967).

VITA

Francis Joaquin Klemm, born on April 28, 1949, is the son of Edward R. and Mary M. Klemm. He attended South Broward High School in Hollywood, Florida.

In 1967 he entered the Florida Institute of Technology in Melbourne. While in attendance he received a Selby Foundation scholarship and was also selected as a member of the Blue Key National Honor Fraternity. His name appears in the 1970-71 edition of Who's Who Among Students in American Colleges and Universities. In June, 1971 Mr. Klemm received a Bachelor of Science degree in Space Technology and graduated with highest honors.

He entered Georgia Institute of Technology in September, 1971 and received an NDEA fellowship to study in the doctoral program. The Master of Aerospace Engineering degree was conferred in August, 1973. He is an associate member of the Society of Sigma Xi.

On June 19, 1971 Mr. Klemm married the former Pamela Sue Burcher of Melbourne, Florida and they have one child, Francis Joaquin, Jr.